

# GEODESICS IN FIBERED LATENT SPACES: A GEOMETRIC APPROACH TO LEARNING CORRESPONDENCES BETWEEN CONDITIONS

TARIQ DAOUDA\*, REDA CHHAIBI\*, PRUDENCIO TOSSOU,  
AND ALEXANDRA-CHLOÉ VILLANI

**ABSTRACT.** This work introduces a geometric framework and a novel network architecture for creating correspondences between samples of different conditions. Under this formalism, the latent space is a fiber bundle stratified into a *base space* encoding conditions, and a *fiber space* encoding the variations within conditions. The correspondences between conditions are obtained by minimizing an energy functional, resulting in diffeomorphism flows between fibers. We illustrate this approach using MNIST and Olivetti and benchmark its performances on the task of batch correction, which is the problem of integrating multiple biological datasets together.

---

## CONTENTS

1. Introduction	2
2. Geometric framework	4
2.1. Fiber bundles	4
2.2. Geodesic transport	5
3. Fibered Auto-Encoders	7
3.1. Auto-encoder definition	7
3.2. Disentangling fiber and base spaces	8
3.3. Ensuring reconstruction quality	9
3.4. Training algorithm	10
4. Applications	10
4.1. The principle of geodesic transport with MNIST	11
4.2. Geodesic interpolation on the Olivetti dataset	12
4.3. Evaluation on single-cell data	13
5. Conclusion	15
Appendix A. On the existence and uniqueness of geodesics	16
A.1. Discussion of the setting and hypotheses	17
A.2. Existence of minimizers	18
A.3. Smoothness of geodesics	19
A.4. Constant speed	20

---

\*: EQUAL CONTRIBUTION

(Daouda and Villani) MASSACHUSETTS GENERAL HOSPITAL, BOSTON, MA & HARVARD MEDICAL SCHOOL, BOSTON, MA & BROAD INSTITUTE, CAMBRIDGE, MA

(Chhaibi) UNIVERSITÉ PAUL SABATIER, TOULOUSE 3 – INSTITUT DE MATHÉMATIQUES DE TOULOUSE (IMT) – 118, ROUTE DE NARBONNE, 31400, TOULOUSE, FRANCE

(Tossou) INVIVOAI, MONTREAL, QC & UNIVERSITÉ LAVAL, QUÉBEC, QC

*E-mail addresses:* [tdaouda@broadinstitute.org](mailto:tdaouda@broadinstitute.org), [reda.chhaibi@math.univ-toulouse.fr](mailto:reda.chhaibi@math.univ-toulouse.fr), [prudencio@invivoai.com](mailto:prudencio@invivoai.com), [avillani@mgh.harvard.edu](mailto:avillani@mgh.harvard.edu).

*Key words and phrases.* Auto-Encoders, Latent variables as a Riemannian fiber bundle, Representation learning.

A.5. Uniqueness	20
A.6. The local diffeomorphism property via a flow	21
A.7. Future directions	22
Appendix B. On the numerics of geodesics	22
B.1. The approximate problem	22
B.2. Regularization	23
B.3. Choices of hyper-parameters	23
B.4. Training hardware	23
Appendix C. Details on the training framework	24
C.1. Domain Adversarial Training	24
C.2. Algorithms	25
C.3. FAE training hardware	27
C.4. Datasets	27
Appendix D. Image datasets experiments	27
D.1. FAE hyper-parameters selection	27
Appendix E. Single-cell RNA sequencing experiments	27
E.1. Classifiers training	27
E.2. FAE hyper-parameters selection	27
E.3. FAE Architectures	27
E.4. scGen architecture	28
E.5. SAUCIE architecture	28
E.6. Metric: LISI (Local Inverse Simpson Index)	28
E.7. Metric: Huygens-Ward variance decomposition	28
Appendix F. Additional figures	29
References	33

---

## 1. INTRODUCTION

Most datasets are naturally stratified in sub-datasets (i.e., populations) by their metadata and annotations. For example, biological datasets could include annotations such as patient age, ethnicity and medical history. Bank transactions could be stratified by gender, time periods, locations.

Conceptually, differences within each population are often due to differences in their generative processes (i.e. in the latent variables that have generated them). Modelling therefore needs to account for sample differences by explicitly disentangling generative latent variables from the condition themselves. This disentanglement is critical for many practical applications such as: understanding the variability factors within each population and understanding the correspondences between samples from different populations.

Current unsupervised methods often fail to consider or neglect this disentanglement. In fact, the distribution of a variable  $x$  stratified by a condition  $c$  is often modelled using latent variables  $z$  as  $p(x|z, c)$  without any considerations for the dependencies between  $z$  and  $c$ . For example, variational approaches such as Conditional Variational Auto-Encoders (CVAEs) [KMRW14, WSL17, LNTW19] typically use bi-modal decoders that take both the latent variables and the condition encodings but do not account for duplication in information between them. Similar architectures are used for Conditional Generative Adversarial Networks (CGAN) [MO14, Ode16, ZPIE17] and hybrid methods mixing GANs and VAE [MSJ<sup>+</sup>15, LSLW15]. The recent paper [Nic19] on the other hand explores models

with explicit disentanglement methods in a VAE framework. The model is however not conditioned and relies instead on a ST-Layer to learn deformations of latent space.

In this work, we propose a geometric formalism that accounts for dependencies between conditions and latent variables with a disentanglement directly implemented at the level of the geometry and the learning. The natural idea is to take a Riemannian fiber bundle  $M$  for latent space. That is to say that  $M$  is stratified into a base space  $B$ , encoding conditions, and a fiber space  $F$ , encoding variations within conditions. Within this formalism samples are encoded using two coordinates  $(f, b) \in B \times F$ .

More importantly, this formalism allows us to compute correspondences between conditions using a natural Riemannian structure on  $M$ . This allow us to reduce the problem of translating samples between two conditions to finding the geodesics (shortest paths) in  $M$  linking their corresponding fibers. We achieve this by minimizing an energy functional, which allow us to calculate diffeomorphism flows between fibers (see Fig. 1.1).

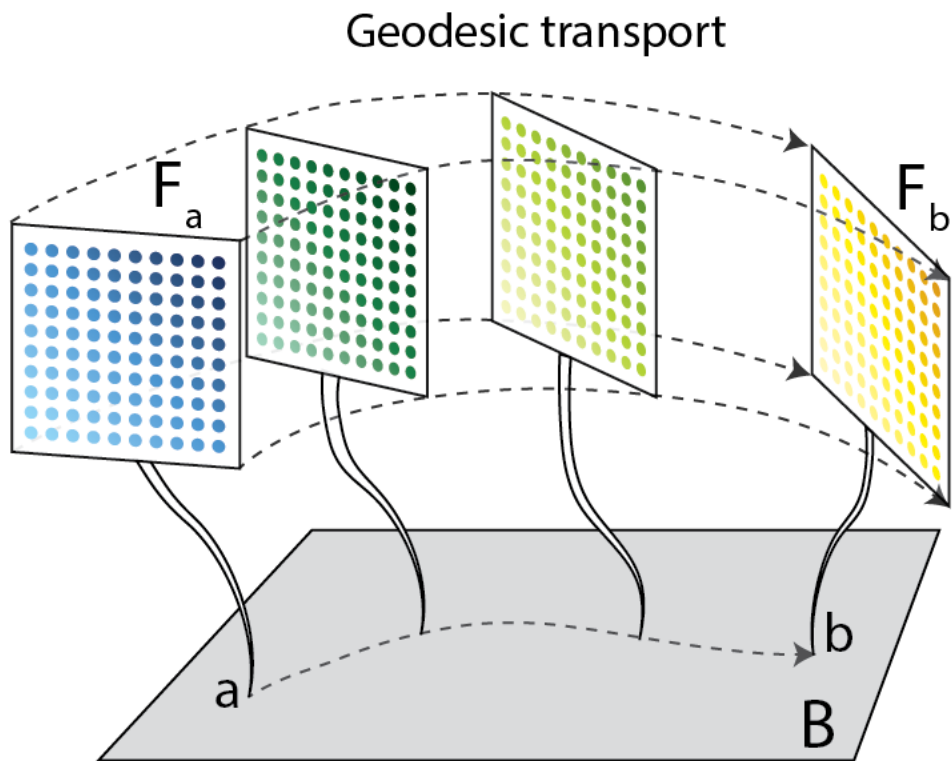


FIGURE 1.1. Conceptual sketch of the proposed method. We stratify the learned latent space  $M$  into a base space  $B$  and a fiber space  $F$ . Under this representation, samples can be formally transported from  $F_a$  to  $F_b$ , and geodesic interpolations between latent spaces  $F_a$  and  $F_b$  can be generated.

Endowing latent spaces with a natural Riemannian geometry has already been explored in machine learning, especially in shape analysis. For a modern review, see [PSF19] and the references therein. Our method for computing similarities bares some similarities with the work of [GSSG12]. There, parallel transport is used in the context of vector bundles to transport features between datasets. Their Fig. 1 is in the spirit of what we propose. Nevertheless, our framework is fundamentally different as we do not assume that fibers carry a linear structure and we compute non-linear correspondences.

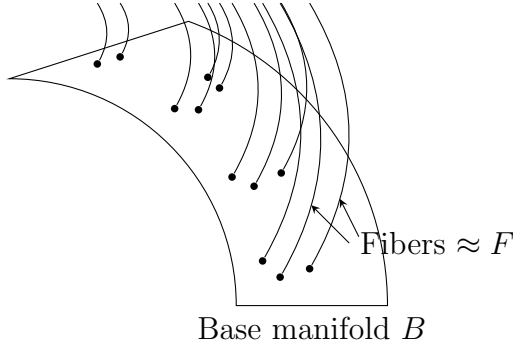


FIGURE 2.1. Illustrative drawing of fiber bundle  $B$  and standard fiber  $F$

We implemented our geometric framework using a non-variational auto-encoder architecture, deemed Fibered Auto-Encoder (FAE). The effectiveness of both FAEs for stratified data modelling, and of the transport method are illustrated by experimenting on MNIST [LC10] and Olivetti [PVG<sup>+</sup>11] datasets.

Finally, we quantify the quality of transport by applying the proposed framework to the batch correction problem. Batch correction refers to the problem of multiple dataset integration in biology. It is a major hurdle preventing researchers from leveraging the power of previously published datasets. We use our approach to translate samples between datasets and provided benchmarks against state of the art methods, including other neural network approaches, and report overall on par, or better results.

## 2. GEOMETRIC FRAMEWORK

We start by explaining how the problem of learning correspondences can be formalized geometrically as geodesically transporting latent variables in a fiber bundle. The only assumption is that there exists a smooth map  $\Psi_\theta$  such that for any coordinates  $(f, b) \in F \times B$ , one can generate samples, via:

$$\hat{X} = \Psi_\theta(f, b) .$$

This function will be later constructed thanks to a neural network.

**2.1. Fiber bundles.** Morally, a fiber bundle  $M$  is a topological space locally stratified along two directions (see Fig. 2.1):

- The horizontal direction is tangent to a topological space called the base manifold  $B$  (in our case encoding conditions).
- The vertical direction is tangent to a topological space called the fiber manifold  $F$  (in our case encoding variations within conditions).

For example, representing the latent space of MNIST as a fiber bundle, the base manifold  $B$  will be an Euclidean space where image labels are embedded. The fiber  $F$  will be the latent space encoding digit variability such as boldness and inclination.

Formally,  $M$  is a fiber bundle with base space  $B$  and fiber  $F$  when,  $M$  is a topological space such that there exists a projection map  $\pi : M \rightarrow B$  such that for every open set  $U \subset B$ ,  $\pi^{-1}(U)$  is diffeomorphic to  $U \times F$  [KSM99]. The fiber sitting above  $b \in B$  is denoted  $F_b := \pi^{-1}(\{b\})$ .

Here we are only concerned with the simplest fiber bundle  $M = B \times F$  where  $\pi$  is the projection on the first coordinate. This space is known as the trivial fiber bundle, as it does not contain any global topological information.

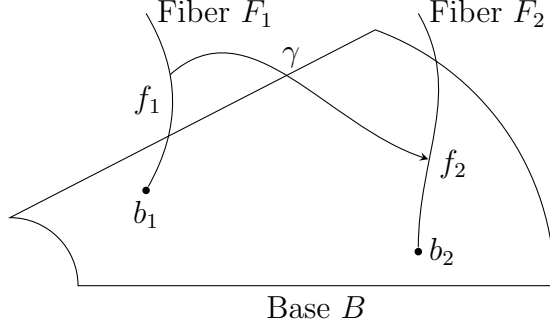


FIGURE 2.2. Illustration of geodesic transport with curve  $\gamma$  from the fiber  $F_1$  to  $F_2$ .

Nevertheless, in general, given  $a \neq b \in B$ , one should not put in correspondence  $F_a = \{a\} \times F$  and  $F_b = \{b\} \times F$  using the identity map on the second coordinate. We refer to this operation as **naive transport**, which is a valid approximation only under certain circumstances. For example, in the case of MNIST, this would amount to considering the spaces encoding the latent properties of 0 and 1 as strictly identical. A priori, spaces of latent properties do change upon changing classes.

We formalize the problem of finding the best correspondence between fibers as a **geodesic transport** problem, which requires the Riemannian point of view developed in the next section 2.2.

**2.2. Geodesic transport.** Our goal is to construct the shortest curves between fibers in  $M$ . This is illustrated in Fig. 2.2. Recall that we assume the existence of a generating process

$$(2.1) \quad \Psi_\theta : M \rightarrow (\mathcal{X}, \|\cdot\|_2) .$$

The target space  $\mathcal{X}$  is taken as Euclidean and endowed with the usual metric  $\|\cdot\|_2$ . The latent space  $M$  however should not be seen as Euclidean. Since the Jacobian  $\nabla \Psi_\theta$  measures the sensitivity with respect to latent variables, it is natural to use it to define a metric on  $M$  where gradients are lower along shorter curves.

A strict mathematical reformulation consists in saying that the latent space  $M$  is given the structure of a Riemannian manifold thanks to a metric tensor  $g$ , by pulling back the metric structure from the generating map  $\Psi_\theta : (M, g) \rightarrow (\mathcal{X}, \|\cdot\|_2)$ . Thus the metric for the latent space  $M$  respects the generative process rather than being the unnatural Euclidean metric on  $M$ .

Let  $n = \dim B$  and  $m = \dim F$ . Given a point  $p \in M$ , we make the identification<sup>1</sup> of the tangent space  $T_p M \simeq \mathbb{R}^{m+n}$ . Also the metric tensor is nothing but the datum of a positive definite matrix  $g(p) \in M_{m+n}(\mathbb{R})$  depending smoothly on the point  $p \in M$ . If  $\langle \cdot, \cdot \rangle$  is the scalar product on  $\mathbb{R}^{m+n}$ , we obtain the Riemannian scalar product  $\langle \cdot, g(p) \cdot \rangle$  on  $T_p M \times T_p M$  for every point. For a curve  $\gamma : [0, 1] \rightarrow M$ , we write  $\gamma_t$  for the position and  $\dot{\gamma}_t \in T_{\gamma_t} M$  for the speed vector at time  $t$ .

By definition, geodesics  $\gamma$  minimize length

$$L(\gamma) = \int_0^1 dt \sqrt{\langle \dot{\gamma}_t, g(\gamma_t) \dot{\gamma}_t \rangle} ,$$

<sup>1</sup>For the sake of simplicity, we adopt the extrinsic point of view throughout the paper, instead of the modern intrinsic point view.

and upon reparametrization, it is well-known that [GHL90][§2.96] geodesics also minimize the energy functional whose general expression is:

$$(2.2) \quad \mathcal{E}(\gamma) := \frac{1}{2} \int_0^1 dt \langle \dot{\gamma}_t, g(\gamma_t) \dot{\gamma}_t \rangle .$$

The energy functional  $\mathcal{E}$  has better convexity properties compared to the length  $L$  and thus its minimization is better behaved numerically. In our case, we choose to define:

$$(2.3) \quad \mathcal{E}(\gamma) := \frac{1}{2} \int_0^1 dt \ |\nabla \Psi_\theta(\gamma_t) \cdot \dot{\gamma}_t|^2 ,$$

which is of the same form as Eq. (2.2) with

$$(2.4) \quad g(p) = \nabla \Psi_\theta(p)^* \nabla \Psi_\theta(p) .$$

Here  $*$  denotes the transposition applied to the Jacobian matrix  $\nabla \Psi_\theta(m)$ . Upon comparing Eq. (2.2) and Eq. (2.3), we see that minimizing the energy  $\mathcal{E}(\gamma)$  with this metric tensor amounts exactly to choosing curves which are causing minimal changes in the output of the generator  $\Psi_\theta$ . Therefore, the role of neural network in the next section is not only to create a space of latent variables but also the geometry of a Riemannian manifold via the metric tensor (2.4).

In the end, the problem of creating correspondences is formalized as follows. Given a  $(f_1, b_1) \in M$  and a point  $b_2 \in B$ , the best corresponding point  $f_2 \in F_{b_2}$  is given by the endpoint of the curve  $\gamma^*$  satisfying the constrained minimization problem:

$$(2.5) \quad \gamma^* = \operatorname{Argmin}_{\substack{\gamma_{t=0}=(f_1, b_1), \\ \gamma_{t=1} \in F_{b_2}}} \mathcal{E}(\gamma)$$

The following theorem states that this problem is often well-posed:

**Theorem 2.1.** *Assume that  $(M, g)$  is path-connected, complete, boundary free and that there exists a universal constant  $C > 0$  such that for all  $p \in M$  and  $v \in T_p M$ :*

$$(H) \quad \frac{1}{C} \|v\|_2^2 \leq \langle v, g(p)v \rangle \leq C \|v\|_2^2 .$$

*Under such hypotheses, minimizing geodesics always exist, are smooth, have constant speed and are generically unique. "Generically" means for all  $(f_1, b_1)$  outside a closed set of zero Lebesgue measure, the cut locus  $\operatorname{Cut}(F_{b_2})$ , while  $b_2$  is fixed.*

*Furthermore, the correspondence*

$$\mathcal{C}_{b_1}^{b_2} : \begin{array}{ccc} F_{b_1} \cap \operatorname{Cut}(F_{b_2})^c & \longrightarrow & F_{b_2} \\ (f_1, b_1) = \gamma_{t=0}^* & \mapsto & (f_2, b_2) = \gamma_{t=1}^* \end{array}$$

*is a well-defined local diffeomorphism between fibers, which tends to the identity map on  $F$  as  $b_1$  converges to  $b_2$ .*

The complete proof is available as supplementary material in Appendix A. Appendix B shows how to numerically implement the minimization in a modern machine learning framework, and discusses the relevance of adding a regularization cost for high dimensional manifolds  $M$ . In applications, we will consider  $B = \mathbb{R}^n$ ,  $F = [-1, 1]^m$  and ignore boundary effects.

### 3. FIBERED AUTO-ENCODERS

A Fibered Auto-encoder (FAE) is essentially a standard auto-encoder whose latent space is stratified into base space  $B$  and a fiber space  $F$ . However, to enforce the disentanglement between  $B$  and  $F$  and to improve the quality of generated samples, we have added auxiliary objectives to the reconstruction loss: (i) to enforce the disentanglement between base and fiber spaces, (ii) to improve the quality of the reconstructions.

Throughout this work, we used only fully-connected layers. The architecture we propose can however accommodate any other types of layers. Throughout this section, we discuss Fig. 3.1 which serves as a comprehensive drawing.

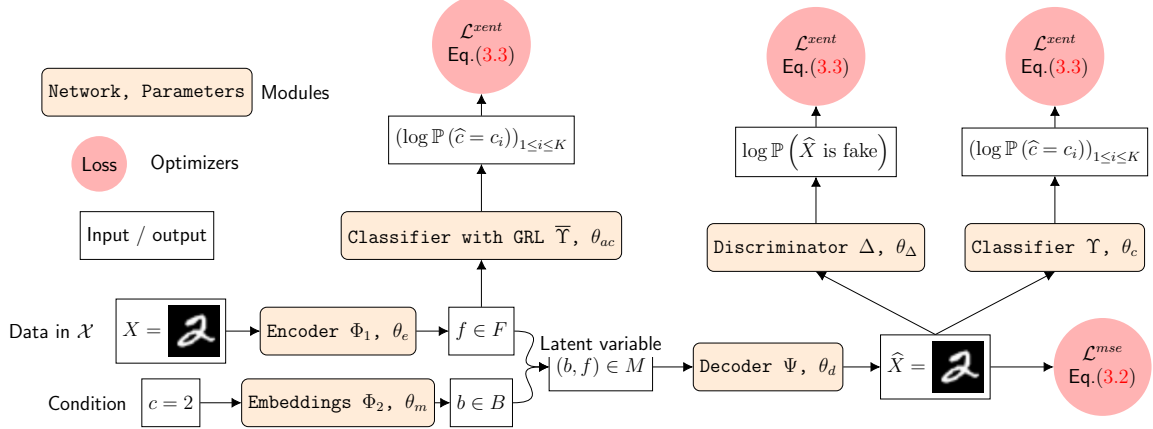


FIGURE 3.1. Network architecture. The general architecture is that of an auto-encoder receiving couples of samples and conditions  $(X, c)$  and outputting a reconstruction  $\hat{X}$ . The latent space is stratified into the fiber coordinate  $f$  (output of the bottleneck layer), and the base coordinate  $b$  encoding conditions. To the auto-encoder architecture we have added the classifier  $\bar{\Upsilon}$  coupled with a GRL to disentangle  $f$  from  $b$ , the GAN discriminator  $\Delta$  to ensure reconstruction realism, and the condition classifier  $\Upsilon$  to prevent mode collapses.

**3.1. Auto-encoder definition.** Just like in a standard auto-encoder [BLPL07, VLL<sup>+</sup>10], the encoder part of an FAE receives the sample  $X$  and terminates in a bottleneck layer with a dimensionality lower than that of the input. The output  $f$  of the bottleneck layer is concatenated with the output  $b$  of an embedding layer that receives the condition label  $c$ . For a pair of sample and condition  $(X, c)$ , the output of the FAE is computed as  $\hat{X} := \Psi_{\theta_d}(f, b)$  with  $f := \Phi_{1, \theta_e}(X)$  and  $b := \Phi_{2, \theta_m}(c)$ . In fact,  $\Psi_{\theta_d}$  is the decoder function used in the previous section.

For convenience, we package all the parameters optimized for reconstruction as  $\theta = (\theta_e, \theta_m, \theta_d)$ . We shall write:

$$(3.1) \quad (f, b) := \Phi_{\theta}(X, c) = (\Phi_{1, \theta_e}(X), \Phi_{2, \theta_m}(c)) .$$

The variable  $f \in F$  represents the coordinates of the sample in the fiber space, while  $b \in B$  represents the coordinates of the condition in the base space.

In accordance with the metric (2.1) of  $\mathcal{X}$ , the reconstruction loss we minimize is the Mean Squared Error (MSE):

$$(3.2) \quad \mathcal{L}^{mse}(\theta ; \mathcal{D}) := \frac{1}{N} \sum_{i=1}^N \left\| X_i - \hat{X}_i \right\|_2^2,$$

where the dataset is  $\mathcal{D} := ((X_i, c_i))_{1 \leq i \leq N}$ .

To help with training we added skip connections that propagate the latent variables  $(f, b)$  to every layer of the decoder. The output  $H_i$  of a decoder's  $i$ -th layer is defined by:

$$H_i := \Psi_{i, \theta_d}(f, b, H_{i-1}).$$

Once trained, samples can be generated from the network by sampling from  $F$  and  $B$  and using the decoder.

Finally, the auto-encoder uses the *sine* function as non-linearity. This is for two reasons: (i) a smooth decoder  $\Psi_\theta$  is needed in order to induce a structure of smooth Riemannian manifold (See Eq. (2.4)). (ii) in contrast to the *sigmoid* and *tanh* functions, the *sine* function has the added advantage of not saturating. Since *sine* outputs are in  $[-1, 1]$ , it follows that  $F = [-1, 1]^n$ , where  $n$  is the number of neurons in the bottleneck.

**3.2. Disentangling fiber and base spaces.** Because the encoder  $\Phi_{1, \theta_e}$  is exposed to the training samples, information about sample condition could become jointly encoded into  $F$  and  $B$ . Fiber and base space would then be entangled, which could hinder both the generative process and the transport. Here we found that the simple addition of a classifier predicting the condition  $c$  from  $F$  coupled with a Gradient Reversal Layer (GRL) worked well in our case (Fig. 3.2). This method was first introduced to disentangle samples from domains [GL14, GUA<sup>+</sup>17]. Other methods explicitly minimizing the mutual information [BBR<sup>+</sup>18] could be explored in the future.

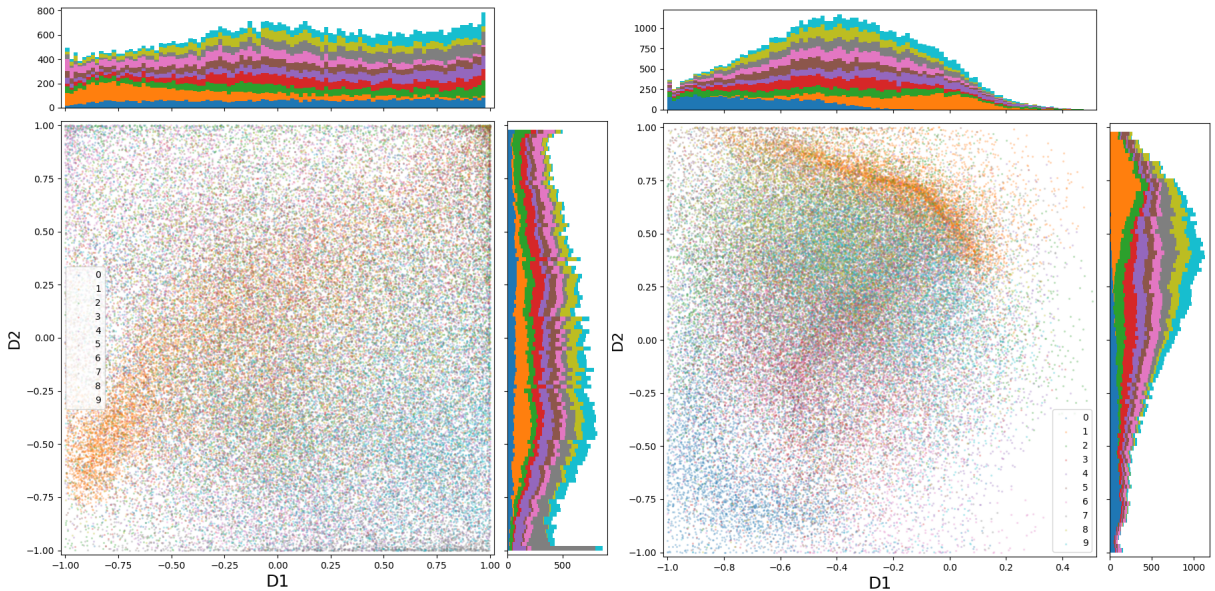


FIGURE 3.2. MNIST fiber space for all conditions. Every digit is a condition represented by a color. Fiber space is  $[-1, 1]^2$ . Left: network trained with condition adversarial training, right: without. Empirical distributions on fibers are closer to uniform, making them less distinguishable.

The classifier  $\bar{\Upsilon}_{\theta_{ac}}$  has output  $\ell := \bar{\Upsilon}_{\theta_{ac}}(f)$ , where  $\ell$  is the vector of log-likelihoods

$$\ell := (\log \mathbb{P}(\hat{c} = c_i))_{1 \leq i \leq n}.$$

$\bar{\Upsilon}_{\theta_{ac}}$  is trained by minimizing the cross-entropy loss with log-likelihoods  $\ell$ , when the real condition is  $c$ :

$$(3.3) \quad \mathcal{L}^{xent}(\ell, c) := -\log \left( \frac{\exp(\ell_{i(c)})}{\sum_{i=1}^n \exp(\ell_i)} \right),$$

where  $i(c)$  is the index of the condition  $c$ .  $\bar{\Upsilon}_{\theta_{ac}}$  is coupled with a GRL at the level of  $f$ . Updates are thus defined as:

$$(3.4) \quad \theta_e \leftarrow \theta_e + \mu_{ac} \lambda \frac{\partial \mathcal{L}^{xent}(\bar{\Upsilon}(f), c)}{\partial \theta_e},$$

$$(3.5) \quad \theta_{ac} \leftarrow \theta_{ac} - \mu_{ac} \lambda \frac{\partial \mathcal{L}^{xent}(\bar{\Upsilon}(f), c)}{\partial \theta_{ac}},$$

The loss (3.3) is thus maximized over  $\theta_{ac}$  and minimized over  $\theta_e$ . We refer to this pass as the *condition adversarial training* update in Algorithm 3.1.

**3.3. Ensuring reconstruction quality.** The loss (3.2) on its own is not necessarily the optimal choice for every application. Having accessory objectives aimed at improving the realism of generated samples is especially important for applications to datasets where the quality of samples cannot be evaluated by the naked eye.

**3.3.1. Ensuring reconstruction realism.** Generative adversarial networks (GANs) [GPAM<sup>+</sup>14] are the state of the art when it comes to generating realistic images [KLA19], and have been shown to improve the quality of reconstruction of auto-encoders [MSJ<sup>+</sup>15]. Here we used a GAN objective to ensure that the samples generated by the FAE are realistic.

GANs involve the joint training of a discriminator network  $D_{\theta_d}$  that learns to discriminate between generated and real samples, and a generator network  $G_{\theta_g}$  that learns to counterfeit more realistic samples. The standard GAN optimization is classically defined as a min-max problem [GPAM<sup>+</sup>14]:

$$\min_{\theta_g} \max_{\theta_d} \mathbb{E} [\log (1 - D_{\theta_d} \circ G_{\theta_g}(Z)) + \log D_{\theta_d}(X)]$$

where the expectation is over the real samples  $X$ , and  $Z$  an input used to generate counterfeited samples. The type of GAN objective can be chosen with respect to the task. To implement the adversarial loss, we add a discriminator  $\Delta$  to the architecture and treat the decoder  $\Psi$  as the generator. Here, we have used a standard GAN approach for images and Wasserstein-GAN (WGAN) [ACB17] for single-cell applications. The use of other GAN types such as MMD GANs [LCC<sup>+</sup>17] could be explored in future work. In Algorithm 3.1 this pass is referred to as *gan update*.

**3.3.2. Ensuring condition discriminative features.** The GAN objective ensures the realism of generated samples, but does not prevent cases of mode collapses where reconstructions can be decoupled from their conditions, and still be deemed realistic by the discriminator. We prevent this by ensuring that the discriminative features of every condition are still present in the reconstructions.

We train a classifier  $\Upsilon_{\theta_c}$  of the condition over real samples, which computes  $\ell := \Upsilon_{\theta_c}(X)$ . It is trained by minimizing the cross-entropy loss with the log-likelihoods  $\ell$  over the real samples  $X$ . We then update the parameters  $\theta_m$  and  $\theta_d$  of respectively,  $\Phi_2$  and  $\Psi$ , to

minimize the cross-entropy of  $\Upsilon_{\theta_c}(\hat{X})$ . We refer to this pass as the *condition fitting update* in Algorithm 3.1.

---

**Algorithm 3.1** FAE Training algorithm

---

**Input:**

dataset:  $\mathcal{D}$

parameters:  $\theta_e, \theta_m, \theta_d, \theta_{ac}, \theta_c, \theta_\Delta$

learning rates:  $\mu_{mse}, \mu_{ac1}, \mu_{ac2}, \mu_{c1}, \mu_{c2}, \mu_{\Delta1}, \mu_{\Delta2}$

**for all**  $(X, c) \in \mathcal{D}$  **do**

$\hat{X} \leftarrow \Psi_{\theta_d}(\Phi_{\theta_e, \theta_m}(X, c))$

reconstruction-update( $X, \hat{X}, \theta_e, \theta_m, \theta_d, \mu_{mse}$ )

$f \leftarrow \Phi_{1\theta_e}(X)$

condition-adversarial-update( $f, c, \theta_e, \theta_{ac}, \mu_{ac1}, \mu_{ac2}$ )

$\hat{X} \leftarrow \Psi_{\theta_d}(\Phi_{\theta_e, \theta_m}(X, c))$

condition-fitting-update( $X, \hat{X}, \theta_d, \theta_m, \theta_c, \mu_{c1}, \mu_{c2}$ )

$\hat{X} \leftarrow \Psi_{\theta_d}(\Phi_{\theta_e, \theta_m}(X, c))$

gan-update( $X, \hat{X}, \theta_e, \theta_m, \theta_d, \theta_\Delta, \mu_{\Delta1}, \mu_{\Delta2}$ )

**end for**

---

**3.4. Training algorithm.** The algorithm we propose (Alg. 3.1) trains the different parts sequentially each with a specific learning rate. By setting different learning rates, one can fine tune the relative importance of the different objectives. Because the main objective is to minimize the reconstruction loss in (3.2), we typically give it the highest learning rate. We used the Adam optimizer [KB14] for all objectives. The details of every sub-routine are given in supplementary material.

#### 4. APPLICATIONS

We first illustrate our method by experimenting on image datasets. We then benchmark the quality of created correspondences on single-cell datasets RNA-sequencing. Throughout this section, we contrast naive transport between two fibers, with geodesic transport.

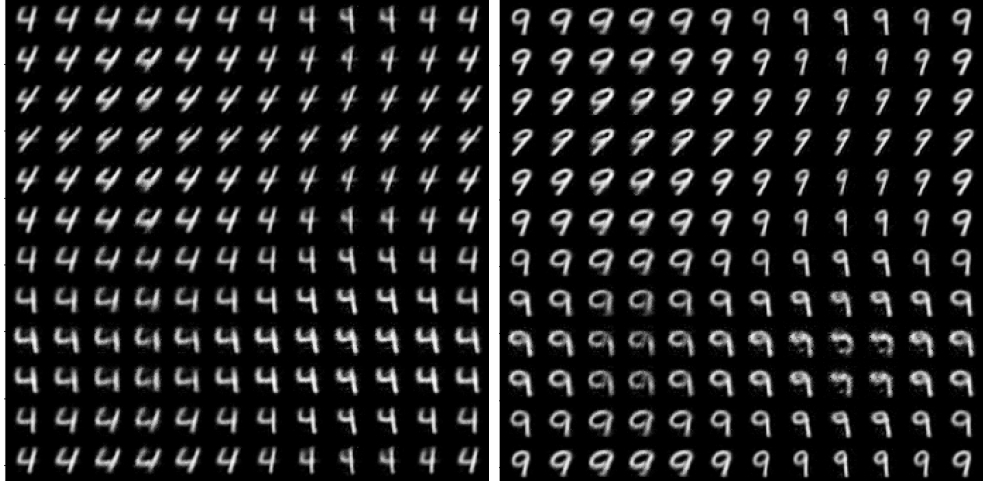


FIGURE 4.1. Manifold plots for the fibers  $F_4$  and  $F_9$  in MNIST. Images were generated using an evenly spaced grid in the standard fiber space  $F = [-1, 1]^2$ .

**4.1. The principle of geodesic transport with MNIST.** We first experiment on MNIST. Here, the possible conditions are the digits  $\{0, 1, \dots, 9\}$ , the base is  $B = \mathbb{R}^2$  and the standard fiber is  $F = [-1, 1]^2$ . Fig. 4.1 shows manifold plots obtained from an evenly spaced grid on  $F_4$  and  $F_9$ . We can see that the reconstructions are of high quality and show a high diversity of samples despite the small bottleneck size (2 units). We also see that the learned latent space is contiguous as any coordinate  $f \in [-1, 1]^2$  yields a realistic digit. Finally, Fig. 4.1 shows that the learned space has an intrinsic organisation, as gradually moving on fibers gradually changes digit features. Manifolds for  $F_4$  and  $F_9$  exhibit similar structures, with points at the same coordinate having similar inclination and boldness. This shows that naive transport is capable of creating rather accurate correspondences between fibers of similar conditions. We do not give the manifold plot after geodesic transport as the difference with naive transport are barely perceivable.

Fig. 4.2 gives an estimation of the diffeomorphism between fibers  $F_4$  and  $F_9$  as formulated in Theorem 2.1. The starting points in  $F_4$  are the orange dots obtained using an evenly spaced grid. The blue dots are the endpoints in  $F_9$  for the calculated geodesics. The diffeomorphism induced through geodesic transport is globally close to the identity. This shows that naive transport can give a good approximation. However, the correction applied by geodesic transport is more apparent as we get closer to the edges.

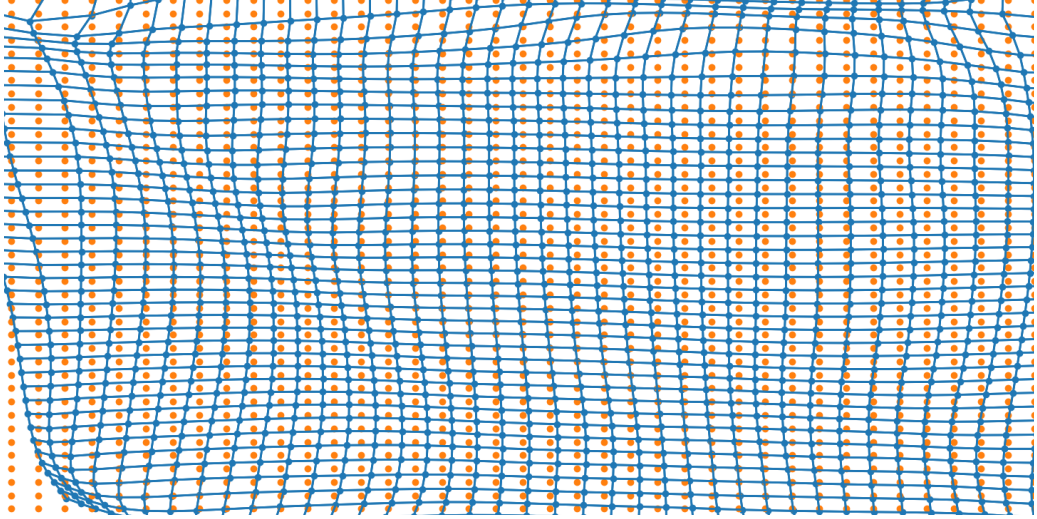


FIGURE 4.2. Diffeomorphism between  $F_4$  and  $F_9$ . The orange dots represent the original coordinates in  $F_4$ , the blue dots are their corresponding images in  $F_9$  computed through geodesic transport.

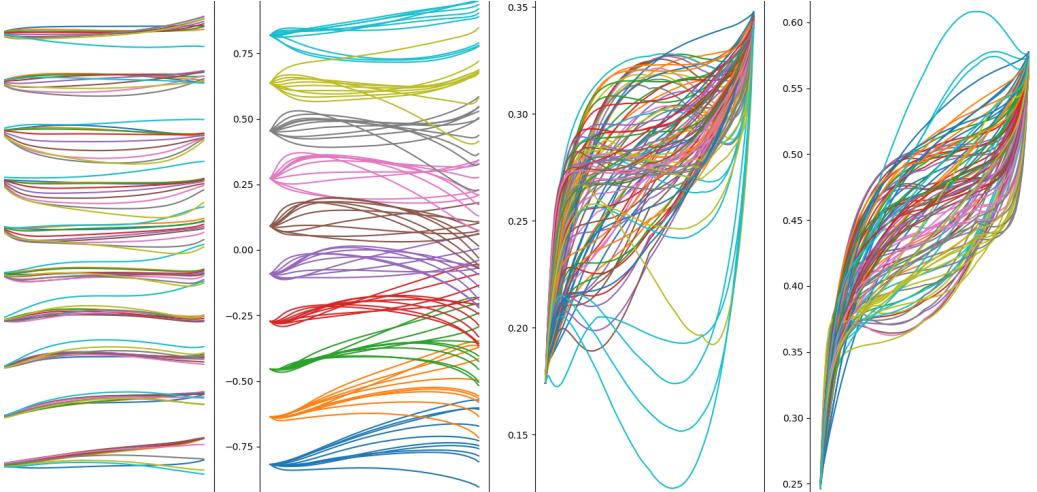


FIGURE 4.3. Geodesics from  $F_4$  to  $F_9$ . The  $x$  axis displays time  $t \in [0, 1]$ . The two left panels display coordinates in fiber space  $F = [-1, 1]^2$  and the two right panels display coordinates on  $B = \mathbb{R}^2$ .

Fig. 4.3 displays a subset of the geodesics between fibers  $F_4$  and  $F_9$  used to generate Fig. 4.2. These are not straight paths at constant speed, which shows the relevance of the Riemannian point of view. As naive transport is a good approximation in this case, geodesics on  $F$  show relatively small variations. Most of the variations happen on  $B$ . This shows that, in the case of MNIST, a change in condition is more fundamental than a change in condition-specific features. Although these adjustments on  $B$  do not change the endpoints, they still have a major impact on the interpolation between fibers.

**4.2. Geodesic interpolation on the Olivetti dataset.** Here, the possible conditions are the 40 different persons in Olivetti. The dataset contains only 10 images for each condition, taken at different angles and with different lighting conditions, making it a challenging dataset for generative networks. Given the very small sample size here we used  $F = [-1, 1]$  as the standard fiber and  $B = \mathbb{R}^{10}$ .

Fig. 4.4 shows generated samples for individuals 8 and 21. Despite the limited dataset size and the very small size of  $F$ , the network is able to generate more samples than in the training set. Individual 8, gradually turns his head, while individual 21 gradually smiles. Fig. 4.5 shows the results of naive and geodesic transport from  $F_8$  to  $F_{21}$ . Interestingly, geodesic transport created more accurate correspondence by hiding the teeth. Finally, Fig. 4.6 shows interpolations along the paths used to generate Fig. 4.5. Individual 8 gradually transforms into individual 21. The network is able to generate faces from intermediary points which shows that it was able to generalize in both  $B$  and  $F$ .



FIGURE 4.4. Olivetti manifold plots. Images generated using an evenly spaced grid on the whole fiber space  $F = [-1, 1]$ , for individuals 8 (top) and 21 (bottom).

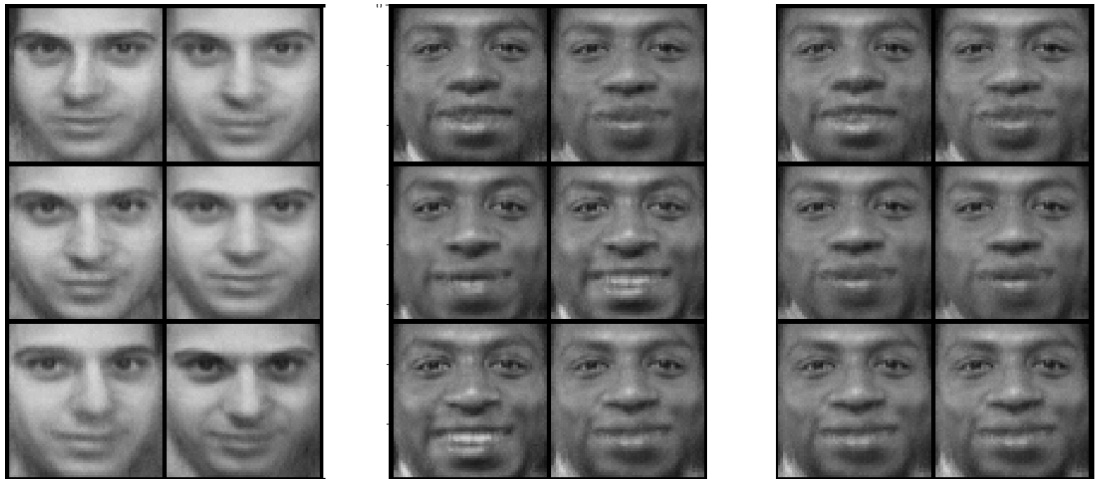


FIGURE 4.5. Calculated correspondences from  $F_8$  to  $F_{21}$ . Starting points on  $F_8$  (left), correspondences calculated through naive transport (center), correspondences calculated through geodesic transport (right). Geodesic transport hides the teeth from subject 21.



FIGURE 4.6. Geodesic interpolation from  $F_8$  to  $F_{21}$ . Individual 8 gradually morphs into individual 21.

**4.3. Evaluation on single-cell data.** Single-cell RNA sequencing measures the gene expression of each cell individually. The result is a matrix where each cell is represented by a vector of gene expressions. However, differences in sample handling and technical platforms leave strong imprints that uniquely mark each batch and overshadow the biology. These imprints are commonly referred to as *batch effects*. The process of *batch correction*

refers to the integration of batches together while preserving relevant biological signal, such as cell types that can be inferred through the expression of distinct gene modules.

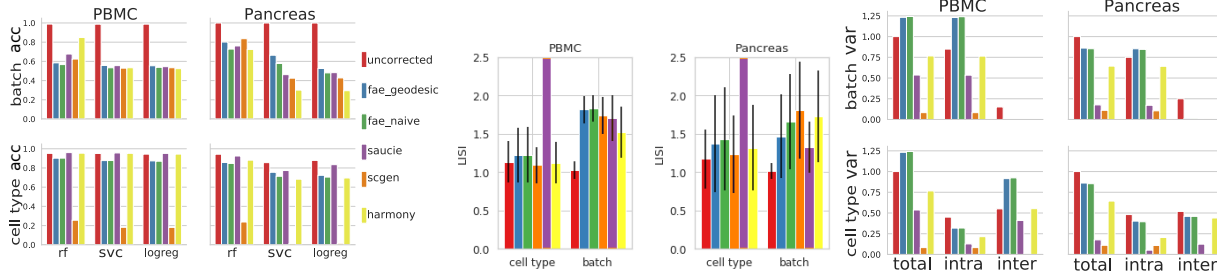


FIGURE 4.7. Left: Accuracies for uncorrected and batch correction methods on both dataset. Batch accuracy (lower is better) and, cell type accuracy (higher is better) are reported for random forest (rf), support vector classifier (svc) and logistic regression (logreg). Middle: LISI scores for uncorrected and batch correction methods on both datasets. LISI on cell type (closer to 1 is better), LISI on batch (higher is better). Error bars display the standard deviation. Right: Total variance and Ward’s variance decomposition, for uncorrected data and batch correction methods. Total variance has been normalized to 1, on the uncorrected dataset.

We use FAEs to represent batches as separate conditions, we then correct the batch effect by transporting all cells to a single reference batch. We benchmark our methods against the current state of the art in batch correction: Harmony [KMF<sup>+</sup>19], and two neural networks developed to handle and batch correct single-cell RNA sequencing data: scGen [LWT19] and SAUCIE [AVDS<sup>+</sup>19]. As Harmony runs on principal components, we ran our benchmarks on PCA reduced data by using the first 20 principal components, in line with the methodology of [TAC<sup>+</sup>20].

We quantify batch correction quality using the prediction accuracies of three classifiers and the batch correction metric LISI [KMF<sup>+</sup>19]. Finally, we use Ward’s variance decomposition to quantify how much changes in variance can be attributed to variations within groups, as opposed to in-between groups [Sap06][p.258]. LISI and Ward’s method are detailed in supplementary material. We benchmark all methods on two datasets. The first contains two batches of Peripheral Blood Mononuclear Cells (i.e., PBMCs): unstimulated and stimulated (with INF- $\beta$ <sup>2</sup>) [KST<sup>+</sup>18]. The second is a compilation of 4 published pancreatic datasets that have been generated by different groups using 4 distinct single-cell RNA sequencing experimental approaches.

A successful correction removes batch imprint and conserves cells biological identity. Therefore we report in Fig. 4.7 the accuracy on predicting the batch (i.e., lower is better) and the accuracy on predicting the cell type (i.e., higher is better). All methods performed well when it comes to removing the batch signal. Despite using a bottle-neck about 10 times lower <sup>3</sup>, our transport method shows results close to to scGen [LWT19]. SAUCIE over-corrected the batch effect at the expense cell type identity. Compared to naive, geodesic transport increases both cell type and batch predictability. For the LISI scores, once again, naive and geodesic transport show results on par with scGen.

<sup>2</sup>Interferon-beta

<sup>3</sup>We used 10 for pancreas and 16 for PBMC vs 100 for scGen.

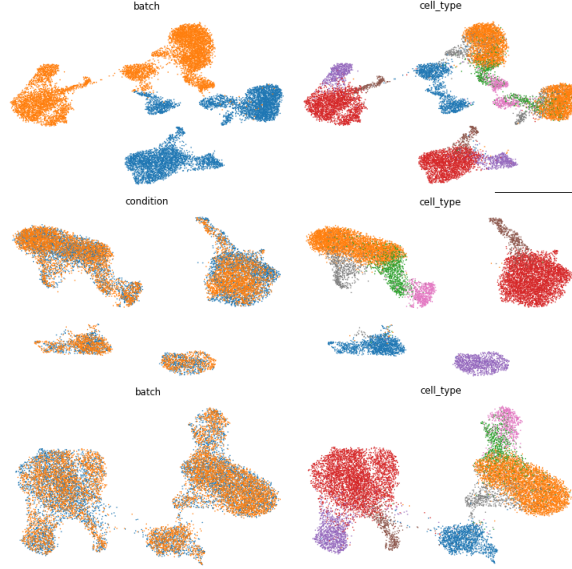


FIGURE 4.8. UMAP visualization of PBMC cells. Left column: cells colored by batch, Right: colored by cell types. From top to bottom: uncorrected data, scGen, geodesic transport (the plot of naive transport is very close to the naked eye). Transport conserves cell types relationships by keeping purple cells (i.e., CD16 monocytes) close to red cells (i.e., CD14 monocytes), which are related to each other.

Ward’s variance decomposition in Fig. 4.7, shows that transport is the only method capable of retaining a significant part of the original variance of the uncorrected dataset. This suggests that our method retains more of the biological signal. On the PBMC datasets, we observe increases in variance within batches and between cell types. Such increases could be due to the network imputing values for missing genes: due to single-cell experimental technical issues, gene expression matrices are very sparse (over 80% to 90%).

Fig. 4.8 shows UMAP plots [MHM18] for uncorrected data, transport and scGen. After correction, batches overlap and cells cluster by cell types. In contrast to scGen, transport kept related cell types, CD16 monocytes (purple) and CD16 monocytes (red), close to each other as in the original uncorrected dataset. This suggest that FAEs are better at conserving relevant structures from datasets, and echoes variance decomposition results (Fig. 4.7).

## 5. CONCLUSION

We proposed: (i) a geometric framework for representation learning which disentangles conditions from sample variations, (ii) a method for computing correspondences between conditions, (iii) a neural network architecture implementing the framework. We restricted ourselves to cases where conditions are of similar nature (e.g. datasets containing the same cell types). Consequently, naive and geodesic transport yield similar results. In turn, one could argue that this proximity morally measures similarity between conditions. Future work could explore applications to more dissimilar conditions and the use of different layer types and loss functions. Finally, the computation of geodesics becomes more challenging as latent space size increases. This technical issue is mitigated by the fact that FAEs can learn accurate representations in very small latent spaces. Nonetheless, addressing it would be a natural follow-up.

Now, for the supplementary material where we will recall some statements of the paper and give more details, for reader's convenience. Also the code is available in an anonymous repository at:

<https://github.com/tariqdaouda/FiberedAE>

## APPENDIX A. ON THE EXISTENCE AND UNIQUENESS OF GEODESICS

In this section, we assume that the latent space  $M$  is a general fiber bundle with standard fiber  $F$  and base space  $B$ . The natural projection is written  $\pi : M \rightarrow B$ . Also we keep the extrinsic point of view by assuming that  $M$  is a submanifold of  $\mathbb{R}^L$  for  $L \in \mathbb{N}$  large enough. By abuse of notation, elements in  $M$  are written  $(f, b) = (f, \pi(f))$  as if we are dealing with a product space. The target space  $\mathcal{X}$  is Euclidean with norm denoted  $\|\cdot\|_2$ . It has a constant metric given by the usual scalar product  $\langle \cdot, \cdot \rangle$ .

Having in mind that  $M$  is the starting space of a generative map

$$\Psi_\theta : M \rightarrow (\mathcal{X}, \|\cdot\|_2) ,$$

the natural metric on  $M$  is given by pullback. See [GHL90][§1.106] for a definition.

**Lemma A.1.** *The pullback metric  $g := \Psi_\theta^* \langle \cdot, \cdot \rangle$  at a point  $p \in M$  identifies to the positive definite matrix*

$$g(p) = \nabla \Psi_\theta(p)^* \nabla \Psi_\theta(p) .$$

*Proof.* Let  $\langle \cdot, \cdot \rangle_p^M$  and  $\langle \cdot, \cdot \rangle_{\Psi_\theta(p)}^{\mathcal{X}}$  be the metrics at  $p \in M$  and  $\Psi_\theta(p) \in \mathcal{X}$ . For any  $p \in M$  and any two tangent vectors  $(x, y) \in T_p M \times T_p M$ , we have by definition of pullback for differential forms:

$$\begin{aligned} \langle x, y \rangle_p^M &= \langle \nabla \Psi_\theta(p)x, \nabla \Psi_\theta(p)y \rangle_{\Psi_\theta(p)}^{\mathcal{X}} \\ &= \langle x, \nabla \Psi_\theta(p)^* \nabla \Psi_\theta(p)y \rangle , \end{aligned}$$

where we used in the last line that  $\mathcal{X}$  is Euclidean. It is indeed of the form  $\langle x, g(p)y \rangle$ .  $\square$

Considering the energy functional  $\mathcal{E}$  for this metric amounts to the following. First consider the energy functional on  $\mathcal{X}$ , whose geodesics are straight lines and which is given for any curve  $c : [0, 1] \rightarrow \mathcal{X}$  by:

$$E(c) = \frac{1}{2} \int_0^1 \|\dot{c}_t\|_2^2 .$$

Then restrict to curves the form  $c_t = \Psi_\theta(\gamma_t)$  where  $\gamma$  is a curve on  $M$ . This naturally yields:

$$\begin{aligned} (A.1) \quad \mathcal{E}(\gamma) &:= \frac{1}{2} \int_0^1 \|\nabla \Psi_\theta(\gamma_t) \dot{\gamma}_t\|_2^2 \\ &= \frac{1}{2} \int_0^1 \langle \dot{\gamma}_t, g(\gamma_t) \dot{\gamma}_t \rangle , \end{aligned}$$

which was our working definition. Notice that after such a restriction, geodesics are not straight lines anymore since  $\text{Im} \Psi_\theta$  is a very small subspace of admissible values.

Let the Sobolev space  $H^1([0, 1]; (M, g))$  be the largest space on which energy is finite:

$$(A.2) \quad H^1([0, 1]; (M, g)) := \{ \gamma : [0, 1] \rightarrow (M, g) \text{ measurable} \mid \mathcal{E}(\gamma) < \infty \} .$$

Given a  $(f_1, b_1) \in M$  and a point  $b_2 \in B$ , this section gives a theoretical treatment of the constrained minimization problem:

$$(A.3) \quad \gamma^* = \operatorname{Argmin}_{\substack{\gamma \in H^1([0,1];(M,g)), \\ \gamma_{t=0} = (f_1, b_1), \\ \gamma_{t=1} \in F_{b_2}}} \mathcal{E}(\gamma) .$$

Recall that we formulated the following theorem:

**Theorem A.2.** *Assume that  $(M, g)$  is path-connected, complete, boundary free and that there exists a universal constant  $C > 0$  such that for all  $p \in M$  and  $v \in T_p M$ :*

$$(H) \quad \frac{1}{C} \|v\|_2^2 \leq \langle v, g(p)v \rangle \leq C \|v\|_2^2 .$$

*Under such hypotheses, minimizing geodesics always exist, are smooth, have constant speed and are generically unique. "Generically" means for all  $(f_1, b_1)$  outside a closed set of zero Lebesgue measure, the cut locus  $\operatorname{Cut}(F_{b_2})$ , while  $b_2$  is fixed.*

Furthermore, the correspondence

$$\begin{aligned} \mathcal{C}_{b_1}^{b_2} : F_{b_1} \cap \operatorname{Cut}(F_{b_2})^c &\longrightarrow F_{b_2} \\ (f_1, b_1) = \gamma_{t=0}^* &\mapsto (f_2, b_2) = \gamma_{t=1}^* \end{aligned}$$

*is a well-defined local diffeomorphism between fibers, which tends to the identity map on  $F$  as  $b_1$  converges to  $b_2$ .*

Before diving into the proof of Theorem A.2, let us comment on the setting and the hypotheses. Then the proof will detail successively the existence of geodesics as minimizers of the energy functional, their smoothness, the fact that they have constant speed, the (generic) uniqueness and finally the local diffeomorphism property.

Although non-trivial, these arguments are classical for a mathematician seasoned in Riemannian geometry.

### A.1. Discussion of the setting and hypotheses.

A.1.1. *On the manifold  $M$ :* Assuming that  $M$  is a path-connected and complete metric space is standard practice, as it avoids many geometric pathologies - see [GHL90][Corollary §2.105]. Also we can assume general fiber bundles. Notice that unlike the setting of vector bundles or  $G$ -principal bundles, our setting has very little equivariance: there is no natural group action preserving the metric on fibers, and there is no natural quotient metric on  $B$ . As such, the convergence of  $b_1 \rightarrow b_2$  so that  $\mathcal{C}_{b_1}^{b_2} \rightarrow \operatorname{id}$  needs to be understood in the Euclidean topology of  $M \subset \mathbb{R}^L$ .

Regarding the setting of manifolds without boundaries, our arguments for existence and smoothness of geodesics carry verbatim to the case of manifolds with boundaries. However, the (already delicate) arguments proving generic uniqueness fail in that case. This is why we made the choice stating a complete theorem with  $M$  having no boundary and we ignored boundary effects in applications.

A.1.2. *Hypothesis (H).* Rather than a complete justification, let us explain why this hypothesis is acceptable in practice.

From the point of view of machine learning, the upper bound on the metric tensor

$$(A.4) \quad g(p) = \nabla \Psi_\theta(p)^* \nabla \Psi_\theta(p)$$

is guaranteed on compact sets as long as  $\Psi_\theta$  is smooth. The lower bound is more delicate. A necessary condition is the non-vanishing gradients (non-saturation) which we already guaranteed thanks to the choice of non-linearities detailed in subsection 3.1. A sufficient

yet reasonable condition is to have  $g(p)$  with full rank and  $g(p)^{-1}$  uniformly bounded. We have to resort to a genericity argument to justify why this is reasonable: since  $\Psi_\theta : M \rightarrow \mathcal{X}$  is a decoder with  $\dim M$  much smaller than  $\dim \mathcal{X}$ , then  $\nabla \Psi_\theta(p)^* \nabla \Psi_\theta(p)$  has rank  $\dim M$  for a generic Jacobian matrix  $\nabla \Psi_\theta(p)$ .

At the level of geometry, it ensures that the manifold's metric  $g$  is comparable (topologically equivalent) to the Euclidean metric  $\|\cdot\|_2$  on  $\mathbb{R}^L$  which contains  $M$ . This yields the inclusion of Sobolev spaces:

$$(A.5) \quad H^1([0, 1]; (M, g)) \subset H^1([0, 1]; \mathbb{R}^L) .$$

The norm of a function  $\varphi \in H^1 := H^1([0, 1]; \mathbb{R}^L)$  is:

$$(A.6) \quad \|\varphi\|_{H^1} := \sqrt{\|\varphi(0)\|_2^2 + \int_0^1 dt \|\varphi'(t)\|_2^2} .$$

**A.2. Existence of minimizers.** For this subsection, we follow the direct method in the calculus of variations [Dac07]. As  $M$  is path connected, the minimization problem (A.3) is over an non-empty set and there exists a minimizing sequence  $(\gamma^n ; n \in \mathbb{N})$  in  $H^1([0, 1]; (M, g))$ . It satisfies:

$$\begin{aligned} \gamma_{t=0}^n &= (f_1, b_1) , \\ \gamma_{t=1}^n &\in F_{b_2} , \\ \mathcal{E}(\gamma^n) &\xrightarrow{n \rightarrow \infty} \inf_{\substack{\gamma \in H^1([0, 1]; (M, g)), \\ \gamma_{t=0} = (f_1, b_1), \\ \gamma_{t=1} \in F_{b_2}}} \mathcal{E}(\gamma) . \end{aligned}$$

The following classical compactness argument allows to find a converging subsequence. First, notice that for all functions  $\varphi \in H^1$  and  $0 \leq t_1 \leq t_2 \leq 1$ :

$$\|\varphi(t_1) - \varphi(t_2)\|_2 \leq \int_{t_1}^{t_2} dt \|\varphi'(t)\|_2 \leq \sqrt{t_2 - t_1} \|\varphi\|_{H^1} ,$$

where we successively used the triangular inequality and the Cauchy-Schwarz inequality. Because of the hypothesis (H) which led to the inclusion (A.5), the sequence  $(\gamma^n, n \in \mathbb{N})$  is bounded in  $H^1$  and the previous inequality shows that  $(\gamma^n, n \in \mathbb{N})$  is equicontinuous and uniformly bounded. Thanks to the Ascoli-Arzela theorem, there exists a subsequence  $n_k$  such that we have the convergence to a continuous path:

$$\gamma^* = \lim_{k \rightarrow \infty} \gamma^{n_k} .$$

This convergence is in the uniform topology and we not know yet that  $\gamma^* \in H^1$ . This is obtained by lower-semicontinuity of the norm function, so that:

$$\|\gamma^*\|_{H^1} \leq \liminf_{k \rightarrow \infty} \|\gamma^{n_k}\|_{H^1} < \infty .$$

Using the same argument for the energy functional:

$$\mathcal{E}(\gamma^*) \leq \liminf_{k \rightarrow \infty} \mathcal{E}(\gamma^{n_k}) = \inf_{\gamma} \mathcal{E}(\gamma) .$$

In the end,  $\gamma^*$  is indeed an energy minimizing geodesic.

**A.3. Smoothness of geodesics.** Let  $(x_k)_{1 \leq k \leq \dim M}$  be a local chart for the manifold  $M$ . Now that we have the existence of a minimizing curves in  $H^1$ , let us write the Euler-Lagrange equation corresponding to the fact that minimizers are critical points of the energy.

To that endeavor, consider a minimizer  $\gamma$  with fixed initial position  $\gamma_{t=0} = (f_1, b_1)$  and fixed final point  $\gamma_{t=1} = (f_2, b_2)$ . We will prove that it necessarily satisfies the Euler-Lagrange equation for all  $t \in [0, 1]$ :

$$(A.7) \quad 0 = \frac{1}{2} \left( \langle \dot{\gamma}_t, \frac{\partial g}{\partial x_k}(\gamma_t) \dot{\gamma}_t \rangle \right)_k - \frac{d}{dt} (g(\gamma_t) \dot{\gamma}_t) .$$

Thanks to the Leibniz rule and rearranging the equation, one obtains the second order ODE:

$$(A.8) \quad g(\gamma_t) \ddot{\gamma}_t = \frac{1}{2} \left( \langle \dot{\gamma}_t, \frac{\partial g}{\partial x_k}(\gamma_t) \dot{\gamma}_t \rangle \right)_k - \frac{d}{dt} (g(\gamma_t)) \dot{\gamma}_t .$$

For any smooth path  $\delta : [0, 1] \rightarrow M$  with  $\delta_0 = \delta_1 = 0$ , which we use as a perturbation, the fact that  $\gamma$  is a critical point yields:

$$\begin{aligned} 0 &= \lim_{\varepsilon \rightarrow 0} \frac{\mathcal{E}(\gamma + \varepsilon \delta) - \mathcal{E}(\gamma)}{\varepsilon} \\ &= \lim_{\varepsilon \rightarrow 0} \frac{1}{2} \varepsilon^{-1} \int_0^1 dt \langle \dot{\gamma}_t + \varepsilon \dot{\delta}_t, g(\gamma_t) \cdot (\dot{\gamma}_t + \varepsilon \dot{\delta}_t) \rangle \\ &\quad + \frac{1}{2} \int_0^1 dt \langle \dot{\gamma}_t + \varepsilon \dot{\delta}_t, \frac{g(\gamma_t + \varepsilon \delta_t) - g(\gamma_t)}{\varepsilon} \cdot (\dot{\gamma}_t + \varepsilon \dot{\delta}_t) \rangle - \frac{1}{2} \int_0^1 dt \varepsilon^{-1} \langle \dot{\gamma}_t, g(\gamma_t) \cdot \dot{\gamma}_t \rangle \\ &= \int_0^1 dt \lim_{\varepsilon \rightarrow 0} \frac{1}{2} \langle \dot{\gamma}_t, \frac{g(\gamma_t + \varepsilon \delta_t) - g(\gamma_t)}{\varepsilon} \cdot \dot{\gamma}_t \rangle + \int_0^1 dt \langle \dot{\gamma}_t, g(\gamma_t) \cdot \dot{\delta}_t \rangle \\ &= \int_0^1 dt \left( \frac{1}{2} \sum_k (\delta_t)_k \langle \dot{\gamma}_t, \frac{\partial g}{\partial x_k}(\gamma_t) \dot{\gamma}_t \rangle + \langle \dot{\gamma}_t, g(\gamma_t) \dot{\delta}_t \rangle \right) . \end{aligned}$$

The above expression assumes that the local chart  $(x_k)_k$  is valid on the entire path. However, this is easily dealt with by taking perturbations  $\delta$  supported on local charts. As such, without loss of generality, we assume for the rest of the argument that the chart is global. Upon performing an integration by parts on the second integral, we obtain:

$$\begin{aligned} 0 &= \int_0^1 dt \left( \frac{1}{2} \sum_k (\delta_t)_k \langle \dot{\gamma}_t, \frac{\partial g}{\partial x_k}(\gamma_t) \dot{\gamma}_t \rangle \right) \\ &\quad + [\langle \dot{\gamma}_t, g(\gamma_t) \dot{\delta}_t \rangle]_0^1 - \int_0^1 dt \left( \sum_k (\delta_t)_k \frac{d}{dt} (g(\gamma_t) \dot{\gamma}_t)_k \right) . \end{aligned}$$

Since  $\delta_0 = \delta_1 = 0$ , the boundary terms  $[\langle \dot{\gamma}_t, g(\gamma_t) \dot{\delta}_t \rangle]_0^1$  vanish. For all smooth  $\delta : [0, 1] \rightarrow M$ , we have:

$$(A.9) \quad 0 = \sum_k \int_0^1 dt (\delta_t)_k \left( \frac{1}{2} \langle \dot{\gamma}_t, \frac{\partial g}{\partial x_k}(\gamma_t) \dot{\gamma}_t \rangle - \frac{d}{dt} (g(\gamma_t) \dot{\gamma}_t)_k \right) .$$

By density of smooth functions in  $L^2([0, 1], M)$ , we obtain:

$$0 = \sum_k \int_0^1 dt \left| \frac{1}{2} \langle \dot{\gamma}_t, \frac{\partial g}{\partial x_k}(\gamma_t) \dot{\gamma}_t \rangle - \frac{d}{dt} (g(\gamma_t) \dot{\gamma}_t)_k \right|^2 ,$$

and the integrand must be zero. This yields indeed the Euler-Lagrange equations (A.7) coordinate-wise.

Multiplying (A.8) by  $g(\gamma_t)^{-1}$ , one sees that  $\ddot{\gamma}$  is a smooth function of  $\dot{\gamma}$  and  $\gamma$ , which is indeed a second order ODE. Because of the Cauchy-Lipschitz Theorem, everything is determined from the datum  $(\gamma_{t=0}, \dot{\gamma}_{t=0})$ . Also because of the ODE's coefficients are smooth, the geodesic  $\gamma$  is smooth as well.

#### A.4. Constant speed.

**Lemma A.3.** *If  $\gamma$  is a geodesic, then necessarily:*

$$\forall t \in [0, 1], \frac{1}{2} \langle \dot{\gamma}_t, g(\gamma_t) \dot{\gamma}_t \rangle = \mathcal{E}(\gamma) .$$

As a consequence, the map  $t \mapsto \frac{1}{2} \int_0^t dt \langle \dot{\gamma}_t, g(\gamma_t) \dot{\gamma}_t \rangle$  grows linearly.

*Proof.* Consider the Euler-Lagrange equation (A.7) and form the scalar product with  $\dot{\gamma}_t$ .

$$0 = -\frac{1}{2} \langle \dot{\gamma}_t, \sum_k (\dot{\gamma}_t)_k \frac{\partial g(\gamma_t)}{\partial x_k} \dot{\gamma}_t \rangle + \langle \dot{\gamma}_t, \frac{d}{dt} (g(\gamma_t) \dot{\gamma}_t) \rangle .$$

Using the chain rule, and then twice the Leibniz rule, we obtain:

$$\begin{aligned} 0 &= -\frac{1}{2} \langle \dot{\gamma}_t, \frac{d}{dt} (g(\gamma_t)) \dot{\gamma}_t \rangle + \langle \dot{\gamma}_t, \frac{d}{dt} (g(\gamma_t) \dot{\gamma}_t) \rangle \\ &= \frac{1}{2} \langle \dot{\gamma}_t, \frac{d}{dt} (g(\gamma_t)) \dot{\gamma}_t \rangle + \langle \dot{\gamma}_t, g(\gamma_t) \ddot{\gamma}_t \rangle \\ &= \frac{1}{2} \frac{d}{dt} \langle \dot{\gamma}_t, g(\gamma_t) \dot{\gamma}_t \rangle . \end{aligned}$$

As such,  $\frac{1}{2} \langle \dot{\gamma}_t, g(\gamma_t) \dot{\gamma}_t \rangle$  is a constant, which is necessarily  $\mathcal{E}(\gamma)$  by virtue of the expression (A.1).  $\square$

An interesting feature of this property is that it can be used to test the convergence of the algorithm described in Section B.

**A.5. Uniqueness.** This is the delicate part. In general, it is well-known that minimizing geodesics are not always unique. The simple example to have in mind is the sphere, where opposite points have infinitely many geodesics joining them i.e great circles. However, pairs of opposite points have zero Lebesgue measure among all possible pairs. This example is in fact archetypal, and the goal of this section is to prove that in most cases of applications, any noise would play in our favor and guarantee unique geodesics.

Now, consider a minimizing geodesic  $\gamma$ , solution to problem (A.3). Necessarily, the geodesic hits the fiber  $F_{b_2}$  along a normal speed. As such, the geodesic can be seen in reversed time by writing  $\tilde{\gamma}_t = \gamma_{1-t}$ . Thus, we obtain a geodesic  $\tilde{\gamma}$  which starts at  $(f_2, b_2)$  with an initial speed normal to  $F_{b_2}$ . Clearly,  $\gamma$  is uniquely determined if and only if  $\tilde{\gamma}$  is uniquely determined among minimal geodesics starting from  $F_{b_2}$  with a normal unit speed and passing through  $(f_1, b_1)$ .

Recall that the the cut locus of a point, written  $\text{Cut}(\{p\})$ , is the set where geodesics starting from  $p \in M$  are no longer minimal - see [GHL90][§2.112]. By [GHL90][Scholium §3.78], non-uniqueness of geodesics starting from  $p$  implies belonging to  $\text{Cut}(\{p\})$ . In fact, as we shall see in the next paragraph, the notion of cut locus generalizes to the case of any closed submanifold  $N$ , which we denote by  $\text{Cut}(N)$ . In our case, we take  $N = F_{b_2}$  and in the end, the proof requires the two following facts:

- $\text{Cut}(N)$  is closed with vanishing Lebesgue measure.

- Uniqueness of geodesics  $\tilde{\gamma}$  is provided as soon as

$$(f_1, b_1) \notin \text{Cut}(N) .$$

We start with proving the first fact as it allows to properly define  $\text{Cut}(N)$ . Let  $UN$  be the unit normal bundle of  $N$  and

$$\pi_N : UN \rightarrow N \subset M$$

be the natural projection in this context. Following [IT01], a unit speed geodesic segment  $\gamma : [0, a] \rightarrow M$  emanating from  $N$  is called an  $N$ -segment if  $t = d(N, \gamma_t)$  where  $d$  is the natural distance on  $(M, g)$ . Also for  $v \in UN$ , define  $\rho(v) \in \mathbb{R}_+ \cup \{\infty\}$  as the cut time:

$$\rho(v) := \sup \{ t \geq 0 \mid \gamma|_{[0,t]} \text{ is an } N\text{-segment} \} .$$

This generalizes the time up to which a geodesic  $c_v : \mathbb{R}_+ \rightarrow M$  starting at a point with a unit speed  $v$  remains minimal. We obtain the definition of the cut locus with respect to a submanifold  $N$  as [IT01][Definition 2.3]:

$$\text{Cut}(N) := \{ c_v(\rho(v)) \mid v \in N, \rho(v) < \infty \} .$$

Then [IT01][Theorem B] yields that  $\rho$  is Lipschitz regular (where finite). Thus  $\text{Cut}(N) \subset M$  is closed and has Hausdorff dimension at most  $\dim M - 1$ , being the graph of a regular function. As such, the cut locus has indeed zero Lebesgue measure.

For the second fact, consider two minimal geodesics  $\tilde{\gamma}_1$  and  $\tilde{\gamma}_2$  exiting  $N$  with a normal unit speed and passing through  $(f_1, b_1)$ . Necessarily, they cross each other transversally at  $(f_1, b_1)$ . One concludes that  $\tilde{\gamma}_1 \neq \tilde{\gamma}_2$  implies  $(f_1, b_1) \in \text{Cut}(N)$  via essentially the same argument as for a point - see the elegant pictorial proof in [GHL90][Fig 2.20].

**A.6. The local diffeomorphism property via a flow.** By uniqueness of the geodesics outside of the cut locus, the map  $\mathcal{C}_{b_1}^{b_2}$  is well-defined. By identifying  $F_{b_1}$  and  $F_{b_2}$  to the standard fiber  $F$ , one can see  $\mathcal{C}_{b_1}^{b_2}$  as a map from an open set of  $F$  to  $F$ . Furthermore, because of hypothesis **(H)**, the Euclidean topology of  $\mathbb{R}^L$  is comparable to  $M$ 's metric and the convergence to the identity map as  $b_1 \rightarrow b_2$  is obvious.

Now, let us deal with the local diffeomorphism property. Since the cut locus  $\text{Cut}(F_{b_2})$  is closed in  $M$ , so is  $\text{Cut}(F_{b_2}) \cap F_{b_1}$  and there is a neighborhood  $U$  of  $(f_1, b_1) \in F_{b_1}$  where the map  $\mathcal{C}_{b_1}^{b_2}$  is well-defined. By uniqueness of minimal geodesics starting from  $F_{b_2}$  in a normal fashion,  $(\mathcal{C}_{b_1}^{b_2})_{|U}$  is injective. In the end, only smoothness and proving an open image needs to be addressed. This is better seen via the following tubular flow argument.

Start by fixing the minimal geodesic  $\gamma^*$  such that:

$$\gamma_{t=0}^* = (f_1, b_1), \quad \gamma_{t=1}^* = (f_2, b_2) = p ,$$

all of the path  $\gamma^*$  does not intersect the cut locus, by definition of  $\text{Cut}(N)$ . By the tubular neighborhood theorem, there exists a neighborhood of the curve  $\gamma^*$  not intersecting the cut locus. In fact, notice that this neighborhood can be taken as an open tube made of flow lines. To that endeavor, let  $-v \in T_p M$  be the unit speed of  $\gamma^*$  at the end point, then consider a small neighborhood  $\mathcal{N}$  of  $(p, v) \in UN = UF_{b_2}$  and its image via the geodesic flow. By restricting further  $\mathcal{N}$  if needed, we obtain a neighborhood of  $\gamma^*$  of smooth geodesic flow lines. Restricting to the flow lines which intersect  $F_{b_1}$  gives a (local) diffeomorphism flow.

**A.7. Future directions.** Regarding the geometric framework in this paper, we restricted ourselves to a Euclidean finite dimensional target space. The correct distance and the correct induced topology is in generally dependent on the domain of application. An interesting infinite dimensional example is given by the Wasserstein distances, which have very desirable properties in imaging. Efficient computations became possible since the introduction of the entropic regularization technique in [Cut13] and the Riemannian geometry of the Wasserstein space is already on a solid mathematical footing via Otto calculus [Vil08][Chapter 15].

Also, we used in applications the hypercube  $F = [-1, 1]^n$  as standard fiber. This is indeed simpler for practical implementation although the theory we just developed works better in a boundary free setting. As such it is natural to consider other manifolds and manifold-valued latent variables have recently been considered in [DFDC<sup>+</sup>18] and [XD18].

## APPENDIX B. ON THE NUMERICS OF GEODESICS

A first possible route is to numerically solve the geodesic second order ODE (A.7), for instance via a standard Euler scheme. This method requires the computation of the metric tensor exactly, and its derivative. Equivalently, because of the expression (A.4), it requires the computation of the Jacobian  $\nabla \Psi_\theta$  and the Hessian  $\nabla^2 \Psi_\theta$  along the geodesic path  $\gamma$ . However, the computation of higher order derivatives is much too costly in automatic differentiation packages such as pyTorch [PGC<sup>+</sup>17] and TensorFlow [AAB<sup>+</sup>15].

**B.1. The approximate problem.** In order to leverage the power of automatic differentiation, we need a method of order 1. As such, we directly implement a gradient descent which minimizes of the energy functional along all paths:

$$(B.1) \quad \operatorname{Argmin}_{\gamma \in H^1([0,1];(M,g))} \mathcal{E}(\gamma) .$$

Recall that in our case of application  $M = F \times B$  with  $B = \mathbb{R}^n$  and  $F = [-1, 1]^m$ . This yields,  $M \subset \mathbb{R}^L$  with  $L = n + m$ . In order to solve the problem numerically, we use several standard approximations. We start by discarding the restriction to paths that are  $M$ -valued. Since  $M$  has non-empty interior inside  $\mathbb{R}^{m+n}$  and is convex, optimal paths on  $\mathbb{R}^{m+n}$  have little chance of exiting  $M$ . The optimization is thus simplified by considering all the  $\gamma \in H^1([0, 1], \mathbb{R}^{n+m})$ . Furthermore, the optimization problem is made finite-dimensional by expanding the path  $\gamma \in H^1([0, 1], \mathbb{R}^{m+n})$  on a Hilbert basis and keeping only finitely many coefficients. This is exactly the spirit of the Ritz-Galerkin method in numerical analysis. Finally, the energy functional is approximated by a Riemann sum with time step  $\Delta t$ . In doing so, we obtain the computable minimizing problem:

$$(B.2) \quad \operatorname{Argmin}_{\gamma \in V_N} \mathcal{E}_{\Delta t}(\gamma) ,$$

where  $V_N \subset H^1([0, 1], \mathbb{R}^{n+m})$  is a finite dimensional space and

$$E_{\Delta t}(\gamma) = \sum_{k=1}^{1/\Delta t} \frac{|\Psi_\theta(\gamma_{(k+1)\Delta t}) - \Psi_\theta(\gamma_{k\Delta t})|^2}{\Delta t} .$$

Let us conclude this section by giving a precise description of the space  $V_N$ . We chose to build it from the Faber-Schauder system

$$(s_0, s_1, s_{j,k})_{j \in \mathbb{N}, k \in \llbracket 0, 2^j - 1 \rrbracket} ,$$

also commonly known as the basis of hat functions - see Eq.(2.3) from [Tri10][Chapter 2]. This is given for  $t \in [0, 1]$  by:

$$\begin{aligned} s_0(t) &= 1, \\ s_1(t) &= t, \end{aligned}$$

and for all  $j \in \mathbb{N}$  and  $k \in \llbracket 0, 2^j - 1 \rrbracket$ :

$$s_{j,k}(t) = 2^{1+\frac{n}{2}} \int_0^t \psi_{n,k}(u) du$$

where  $\psi_{j,k}$  is the Haar system defined from the Haar wavelet  $\psi = \mathbb{1}_{[0, \frac{1}{2}]} - \mathbb{1}_{[\frac{1}{2}, 1]}$  as

$$\psi_{j,k}(t) = 2^{\frac{n}{2}} \psi(2^n t - k) .$$

The Haar system along with the constant function 1 forms an orthonormal basis of  $L^2([0, 1], \mathbb{R})$ . Therefore, given the norm definition in Eq. (A.6), the Faber-Schauder system is an orthonormal basis of  $H^1([0, 1], \mathbb{R})$ . Upon tensoring, we readily obtain a basis of  $H^1([0, 1], \mathbb{R}^{n+m})$  indexed by triple indices  $(i, j, k)$ :

$$\forall t \in [0, 1], \quad s_{j,k}^i(t) := \sum_{i=1}^{\dim M} s_{j,k}(t) e_i ,$$

where  $(e_i)_{1 \leq i \leq \dim M}$  is the canonical basis of  $\mathbb{R}^{\dim M}$ . In the end, we worked with

$$\begin{aligned} V_N := \text{Span}_{\mathbb{R}} \{ & s_{j,k}^i \mid i \in \llbracket 1, \dim M \rrbracket, \\ & j \in \llbracket 0, N-1 \rrbracket, 0 \leq k < 2^j \} , \end{aligned}$$

and we have:

$$\dim V_N = (2^N + 1) \dim M .$$

**B.2. Regularization.** We have found that the computation of geodesics becomes unstable in the case of high dimensional latent spaces. To solve the problem, we introduced a regularization cost so that instead of minimizing the energy functional  $\mathcal{E}(\gamma)$  among admissible curves, we minimize a loss:

$$\mathcal{L}(\gamma) = \mathcal{E}(\gamma) + \lambda_{\text{reg}} \|\gamma_{t=1} - \gamma_{t=1}^{\text{naive}}\|_2^2 .$$

Here  $\gamma_{t=1}^{\text{naive}} = (f_1, b_2)$  is the result of naive transport. Thanks to the additional term, minimizing curves do not stray too far from the results given by naive transport.

**B.3. Choices of hyper-parameters.** The parameters tracked in the automatic differentiation framework are the coefficients of  $\gamma \in V_N$ . For numerical experiments, we used  $\Delta t = 1/256$  and  $N = 6$ . The gradient descent used the classical RMSprop stepper in pyTorch.

A case-by-case description of learning rates and regularization parameters  $\lambda_{\text{reg}}$  is available in JSON format:

[https://github.com/tariqdaouda/FiberedAE/tree/master/demos/geodesics\\_configurations](https://github.com/tariqdaouda/FiberedAE/tree/master/demos/geodesics_configurations)

**B.4. Training hardware.** Computation of geodesics can be done in parallel for each geodesic separately, on independent copies of the trained neural network. In this context, we simply use multiple CPU threads and our machine of choice was a server with 192 cores Intel Xeon CPU E7-8890 v4 @ 2.20GHz and 512 GB of RAM. This is especially useful for batch correction since datasets come with tens of thousands cells and we needed one geodesic per cell. Otherwise, in order to compute geodesics in the hundreds as in the paper's Fig. 4.3, a laptop is more than enough.

## APPENDIX C. DETAILS ON THE TRAINING FRAMEWORK

In this section we first introduce more thoroughly the works of Ganin et al.[GL14, GUA<sup>+</sup>17] on domain adaptation. We then give a detailed description of the training algorithms, the computer hardware and the datasets.

**C.1. Domain Adversarial Training.** The goal of [GL14, GUA<sup>+</sup>17] was to make a classifier insensitive to changes in the domain of input. Here changing domains manifests in shifts in data distributions that are not related to the nature of the classification task. For a digit classifier, hand-written numbers and house numbers are two possible domains. In that case, being domain insensitive means that the classifier uses discriminating features that are domain independent.

For an input couple data-label  $(X, y)$ , say a picture of a digit and its label, Ganin et al. define a latent variable  $f$  and an estimated label  $\hat{y}$  as follows:

$$(C.1) \quad f := E_{\theta_e}(X) ,$$

$$(C.2) \quad \hat{y} := LC_{\theta_c}(f) = LC_{\theta_c} \circ E_{\theta_e}(X) ,$$

where  $E_{\theta_e}$  is an encoder, and  $LC_{\theta_c}$  a label classifier.

The presence of domain information in the latent space is estimated by adding a domain classifier  $DC_{\theta_d}$  that takes a latent variable  $f$  as input and predicts the domain  $\hat{d}$  from it.

$$(C.3) \quad \hat{d} := DC_{\theta_d}(f) = DC_{\theta_d} \circ E_{\theta_e}(X) .$$

In this context, there are two loss functions:  $\mathcal{L}_{LC}(\theta_e, \theta_c)$  for the label classifier and  $\mathcal{L}_{DC}(\theta_e, \theta_d)$  for the domain classifier. As explained in [GL14][Fig 1], removing domain information from the latent variable is reduced to minimizing  $\mathcal{L}_{LC}$  with respect to  $(\theta_e, \theta_e)$ , minimizing  $\mathcal{L}_{DC}$  with respect to  $\theta_d$  while maximizing it with respect to  $\theta_e$ .

By defining an aggregate loss on the sample  $((X_i, y_i))_{1 \leq i \leq n}$  that is:

$$(C.4) \quad \begin{aligned} \mathcal{L}^{adv}(\theta_e, \theta_c, \theta_d ; ((X_i, y_i))_{1 \leq i \leq n}) \\ := \mathcal{L}_{LC}(\theta_e, \theta_c) - \lambda \mathcal{L}_{DC}(\theta_e, \theta_d) , \end{aligned}$$

we need to implement the saddle-point optimization program that computes  $(\hat{\theta}_e, \hat{\theta}_c, \hat{\theta}_d)$ :

$$(C.5) \quad \left( \hat{\theta}_e, \hat{\theta}_c \right) := \underset{\theta_e, \theta_c}{\text{Argmin}} \mathcal{L}^{adv} \left( \theta_e, \theta_c, \hat{\theta}_d \right)$$

$$(C.6) \quad \hat{\theta}_d := \underset{\theta_d}{\text{Argmax}} \mathcal{L}^{adv} \left( \hat{\theta}_e, \hat{\theta}_c, \theta_d \right)$$

That is found using the sequential stochastic updates given in [GL14][Eq. 4, 5, 6]:

$$(C.7) \quad \theta_e \leftarrow \theta_e - \mu \left( \frac{\partial \mathcal{L}_{LC}}{\partial \theta_e} - \lambda \frac{\partial \mathcal{L}_{DC}}{\partial \theta_e} \right) ,$$

$$(C.8) \quad \theta_c \leftarrow \theta_c - \mu \frac{\partial \mathcal{L}_{LC}}{\partial \theta_c} ,$$

$$(C.9) \quad \theta_d \leftarrow \theta_d - \mu \frac{\partial \mathcal{L}_{DC}}{\partial \theta_d} ,$$

where  $\mu > 0$  is a given learning rate.

A great contribution of Ganin et al. is to recast these non-standard updates as a classical gradient descent, which can be implemented in most deep learning frameworks. This is achieved using a Gradient Reversal Layer (GRL) at the level of  $f$ , that replaces  $\frac{\partial \mathcal{L}_d}{\partial \theta_e}$  with

its opposite. A GRL  $R_\lambda$  seamlessly outputs the identity map during the forward pass, while reversing (and scaling) the gradient during the back-propagation pass. The authors carefully refer to  $R_\lambda$  as a "pseudo-function" and define it as:

$$(C.10) \quad \begin{cases} R_\lambda(x) &:= x, \\ \nabla R_\lambda(x) &:= -\lambda \text{Id}. \end{cases}$$

where  $\text{Id}$  is the identity matrix. The notation is clearly abusive as the two expressions are incompatible for a mathematical function, while perfectly authorized for a neural network layer.

**C.2. Algorithms.** This section shows the details of training an FAE with the algorithm of each sub-routine presented in details. We denote by  $\text{Adam}(\mu, g)$  a step obtained by the Adam gradient descent algorithm, with learning rate  $\mu$  and gradient  $g$ . Besides the learning rate, we used the defaults of pyTorch v.1.4.0 for all other Adam parameters.

---

**Algorithm C.1** FAE reconstruction training algorithm for one batch

---

**Name:** reconstruction-update

**Input:**

Training data:  $(X, \hat{X})$ ,

Parameters:  $\theta$

Learning rates:  $\mu$

$$g_\theta \leftarrow \nabla_\theta \frac{1}{n} \sum_{i=1}^n |X_i - \hat{X}_i|^2$$

$$\theta \leftarrow \theta - \text{Adam}(\mu, g_\theta)$$


---

---

**Algorithm C.2** FAE condition adversarial training algorithm for one batch

---

**Name:** cond-adv-update

**Input:**

Training data:  $f, c$

Parameters:  $\theta_e, \theta_{ac}$

Learning rates:  $\mu_{ac1}, \mu_{ac2}$

$$\ell \leftarrow \overline{\Upsilon}_{\theta_{ac}}(f)$$

$$g_{ac} \leftarrow \nabla_{\theta_{ac}} \left( -\log \left( \frac{\exp(\ell_c)}{\sum_{i=1}^n \exp(\ell_i)} \right) \right)$$

$$\theta_{ac} \leftarrow \theta_{ac} - \text{Adam}(\mu_{ac1}, g_{ac})$$

$$g_e \leftarrow \nabla_{\theta_e} \left( -\log \left( \frac{\exp(\ell_c)}{\sum_{i=1}^n \exp(\ell_i)} \right) \right)$$

$$\theta_e \leftarrow \theta_e + \text{Adam}(\mu_{ac2}, g_e)$$


---

---

**Algorithm C.3** FAE condition fitting algorithm for one batch

---

**Name:** cond-fitting-update**Input:**Training data:  $X, \hat{X}, c$ Parameters:  $\theta_d, \theta_m, \theta_c$ Learning rates:  $\mu_{c1}, \mu_{c2}$  $\ell \leftarrow \Upsilon_{\theta_c}(X)$ 

$$g_{\theta_c} \leftarrow \nabla_{\theta_c} \left( -\log \left( \frac{\exp(\ell_c)}{\sum_{i=1}^n \exp(\ell_i)} \right) \right)$$

$$\theta_c \leftarrow \theta_c - \text{Adam}(\mu_{c1}, g_{\theta_c})$$

$$\hat{\ell} \leftarrow \Upsilon_{\theta_c}(\hat{X})$$

$$g_{d,m} \leftarrow \nabla_{\theta_d, \theta_m} \left( \log \left( \frac{\exp(\hat{\ell}_c)}{\sum_{i=1}^n \exp(\hat{\ell}_i)} \right) \right)$$

$$(\theta_d, \theta_m) \leftarrow (\theta_d, \theta_m) - \text{Adam}(\mu_{c2}, g_{d,m})$$

---

---

**Algorithm C.4** FAE GAN training algorithm for one batch

---

**Name:** gan-update**Input:**training data:  $(X, \hat{X}, c)$ ,parameters:  $\theta_e, \theta_m, \theta_d, \theta_\Delta$ learning rates:  $\mu_{\Delta 1}, \mu_{\Delta 2}$ 

$$g_{\theta_{gd}} \leftarrow \nabla_{\theta_\Delta} \frac{1}{n} \sum_{i=1}^n [\log D(x_i) + \log(1 - D(\hat{x}_i))]$$

$$\theta_\Delta \leftarrow \theta + \text{Adam}(\mu_{\Delta 1}, g_{\theta_\Delta})$$

$$\theta \leftarrow (\theta_e, \theta_m, \theta_d)$$

$$g_\theta \leftarrow \nabla_{\theta} \frac{1}{n} \sum_{i=1}^n \log(1 - D(\hat{x}_i))$$

$$\theta \leftarrow \theta - \text{Adam}(\mu_{\Delta 2}, g_\theta)$$

---

For the reader's convenience, we recall in Algorithm C.5 how the previous algorithms are put together in the training of the entire neural network.

---

**Algorithm C.5** FAE Training algorithm

---

**Input:**dataset:  $\mathcal{D}$ parameters:  $\theta_e, \theta_m, \theta_d, \theta_{ac}, \theta_c, \theta_\Delta$ learning rates:  $\mu_{mse}, \mu_{ac1}, \mu_{ac2}, \mu_{c1}, \mu_{c2}, \mu_{\Delta 2}, \mu_{\Delta 2}$ **for all**  $(X, c) \in \mathcal{D}$  **do**

$$\hat{X} \leftarrow \Psi_{\theta_d}(\Phi_{\theta_e, \theta_m}(X, c))$$

reconstruction-update( $X, \hat{X}, \theta_e, \theta_m, \theta_d, \mu_{mse}$ )

$$f \leftarrow \Phi_{1\theta_e}(X)$$

condition-adversarial-update(  $f, c, \theta_e, \theta_{ac}, \mu_{ac1}, \mu_{ac2}$  )

$$\hat{X} \leftarrow \Psi_{\theta_d}(\Phi_{\theta_e, \theta_m}(X, c))$$

condition-fitting-update(  $X, \hat{X}, \theta_d, \theta_m, \theta_c, \mu_{c1}, \mu_{c2}$  )

$$\hat{X} \leftarrow \Psi_{\theta_d}(\Phi_{\theta_e, \theta_m}(X, c))$$

gan-update( $X, \hat{X}, \theta_e, \theta_m, \theta_d, \theta_\Delta, \mu_{\Delta 1}, \mu_{\Delta 2}$ )**end for**

---

**C.3. FAE training hardware.** All FAEs were trained on a single GPU on a Dell Precision 5530. RAM: 31GiB, CPU: Intel(R) Core(TM) i7-8850H CPU @ 2.60GHz, GPU: Quadro P2000 Mobile.

#### C.4. Datasets.

**C.4.1. Image datasets.** We used the version of MNIST [LC10] provided by pyTorch and the version of Olivetti provided by scikit-learn [PVG<sup>+</sup>11].

**C.4.2. Single cell datasets pre-processing.** We used the version of the pancreas dataset provided by [LWT19] dataset size is (14, 693, 2448). For the PBMC dataset [KST<sup>+</sup>18], we downloaded the pre-normalized version of the dataset provided by [LNTW19]. We normalized gene expressions per cell, transformed expressions using  $\log(expression + 1)$ , and used only the top 2000 highly variable genes after processing dataset size was: (13576, 2000).

For FAE training, all expressions for all datasets were normalized in  $[0, 1]$  by subtracting the minimum value and dividing by the maximum value. As Harmony runs on principal components, we run our benchmarks on PCA reduced data by using the first 20 principal components, in line with the methodology introduced by [TAC<sup>+</sup>20].

## APPENDIX D. IMAGE DATASETS EXPERIMENTS

**D.1. FAE hyper-parameters selection.** All FAEs hyper-parameters were optimized using grid search, with reconstruction learning rates at least 10 times bigger than the highest second learning rate. We considered the following:

- Learning rates:  $(10^{-3}, 2.10^{-3}, 10^{-4}, 2.10^{-4}, 10^{-5}, 2.10^{-5}, 10^{-6}, 2.10^{-6})$ .
- Hidden layer sizes: (64, 128, 256).
- Bottleneck (fiber) sizes: (1, 2, 5, 8, 10, 16, 32).
- Depths: (10, 20, 30, 40, 50, 80, 100).
- Embedding sizes (dim  $B$ ): (1, 2, 10).

## APPENDIX E. SINGLE-CELL RNA SEQUENCING EXPERIMENTS

**E.1. Classifiers training.** We used three classifiers from sklearn v0.22 [PVG<sup>+</sup>11]: Logistic regression (*LogisticRegression*, with solver *lbfgs*), Support vector classifier (*SVC* with kernel *rbf*), random forest (*RandomForestClassifier* with 500 estimators). For all other hyper-parameters we used the defaults of sklearn v0.22.

All classifiers were trained with class balancing and were tested on a randomly selected test set containing 25% of the total dataset.

**E.2. FAE hyper-parameters selection.** All FAEs hyper-parameters were optimized using grid search, with reconstruction learning rates at least 10 times bigger than the highest second learning rate. We considered the following:

- Learning rates:  $(10^{-3}, 2.10^{-3}, 10^{-4}, 2.10^{-4}, 10^{-5}, 2.10^{-5}, 10^{-6}, 2.10^{-6})$ .
- Hidden layer sizes: (64, 128, 256).
- Bottleneck sizes: (1, 2, 5, 8, 10, 16, 32).
- Depths: (10, 20, 30, 40, 50, 80, 100).
- Embedding sizes (dim  $B$ ): 2 for pancreas and 1 for PBMC.

**E.3. FAE Architectures.** All architectures are available in JSON format at:  
<https://github.com/tariqdaouda/FiberedAE/tree/master/demos/configurations>

**E.4. scGen architecture.** We used the following hyper-parameters:

- z\_dimension: 100
- learning\_rate: 0.001
- dropout\_rate: 0.2
- alpha: 0.00005

**E.5. SAUCIE architecture.** We trained this model using the following hyper-parameters:

- lambda\_b=0.1,
- lambda\_c=0,
- layer\_c=0,
- lambda\_d=0,
- layers=[512, 256, 128, 2],
- activation=*ReLU*,
- learning\_rate=0.001

**E.6. Metric: LISI (Local Inverse Simpson Index).** LISI measures the inverse Simpson Index in the local neighbourhood of each cell. Because it is a per-cell measure, here we reported the aggregated mean and standard deviation metrics over all cells. We used the implementation of [KMF<sup>+</sup>19].

For a given cell its LISI score is computed as follows. Let  $S$  be the inverse Simpson index:

$$S = \frac{1}{\sum_{i=1}^Z p(i)}$$

where  $Z$  is the number of batches in the dataset, and  $p(i)$  the probability of the batch  $i$  being present in the local neighbourhood of that cell. To define the neighbourhood of cells, probabilities are computed using a gaussian kernel centered over each cells (here we used a perplexity of 30 as suggested by [KMF<sup>+</sup>19]). The resulting  $S$  is the average number of cells needed to be sampled before two cells from the cell batch are drawn. In a unmixed dataset the LISI score for most cells is close to 1, as it only takes on average 1 draw to a get cell from the same batch. In a well mixed dataset the value should be close to the total number of batches.

Just like [KMF<sup>+</sup>19] we used two versions of the LISI score. One on the batch, and one on the cell-type. Both score are computed in the exact same way, they are however interpreted differently. As the LISI score on batches should increase to become closer to the number of batches, the LISI score on cell-types should remain close to 1. This is because cells of the same types should remain clustered together after correction. An increase in the LISI score on cell-types indicates a loss of cell-type specific features and therefore of relevant biological information.

**E.7. Metric: Huygens-Ward variance decomposition.** Consider a sample

$$\{X_1, \dots, X_N\} \subset \mathbb{R}^n$$

which can be clustered into  $k$  groups ( $G_i$  ;  $1 \leq i \leq k$ ). By definition, the global sample mean and variance are:

$$\begin{aligned} m &:= \frac{1}{N} \sum_{i=1}^N X_i, \\ \sigma^2 &:= \frac{1}{N} \sum_{i=1}^N \|X_i - m\|_2^2. \end{aligned}$$

On the one hand, assimilating each group  $G_j$  to its center of mass

$$m_j := \frac{1}{|G_j|} \sum_{X_i \in G_j} X_i ,$$

the inter-class variance is defined as:

$$\sigma_e^2 := \frac{1}{k} \sum_{j=1}^k \|m_j - m\|^2 .$$

On the other hand, considering each group separately, intra-class variances for each group  $G_j$  are given by:

$$\sigma_j^2 := \frac{1}{|G_j|} \sum_{X_i \in G_j} \|X_i - m_j\|_2^2 .$$

Here  $|G_j|$  stands for the cardinal of the group  $G_j$ . The intra-class variance is defined as:

$$\sigma_a^2 := \frac{1}{k} \sum_{j=1}^k \sigma_j^2 .$$

In the end, performing a conditioning with respect to the groups, we invoke the law of total variance. We obtain that total variance decomposes into the sum of inter-class variance and intra-class variance:

$$(E.1) \quad \sigma^2 := \sigma_e^2 + \sigma_a^2 .$$

This is also known as the Huygens-Ward decomposition of the variance. Such a decomposition has a very clear statistical interpretation for the purposes of batch correction. Grouping the cells by batch, the goal is to minimize the inter-class variance while not destroying the intra-class variance. Grouping the cells by cell-type, the goal is maximizing cell separability by increasing inter-class variance.

## APPENDIX F. ADDITIONAL FIGURES

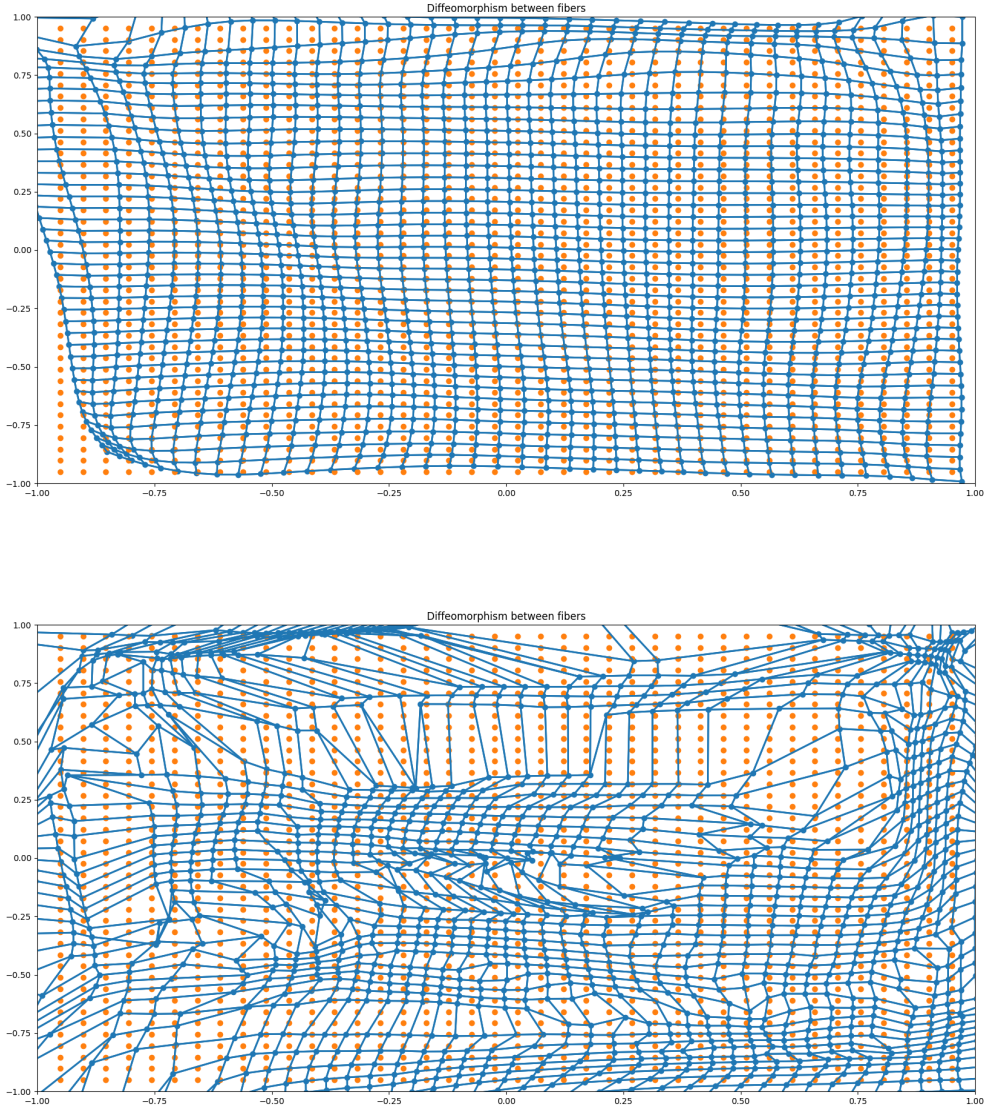


FIGURE F.1. Visualization of the (local) diffeomorphisms between two fibers. Top: From  $F_4$  to  $F_9$ . Bottom: From  $F_1$  to  $F_0$ . Orange dots represent the original coordinates in respectively  $F_4$  and  $F_1$ , blue dots represent the correspondences computed through geodesic transport. In accordance with intuition, the correspondence between  $F_4$  and  $F_9$  is much more global as these digits are more similar. The correspondence between  $F_1$  and  $F_0$  is only locally stable, and shows more "shearing" and "tearing". The bottom picture is already stabilized thanks to a regularization parameter  $\lambda_{\text{reg}} = 0.02$  (See subsection B.2).

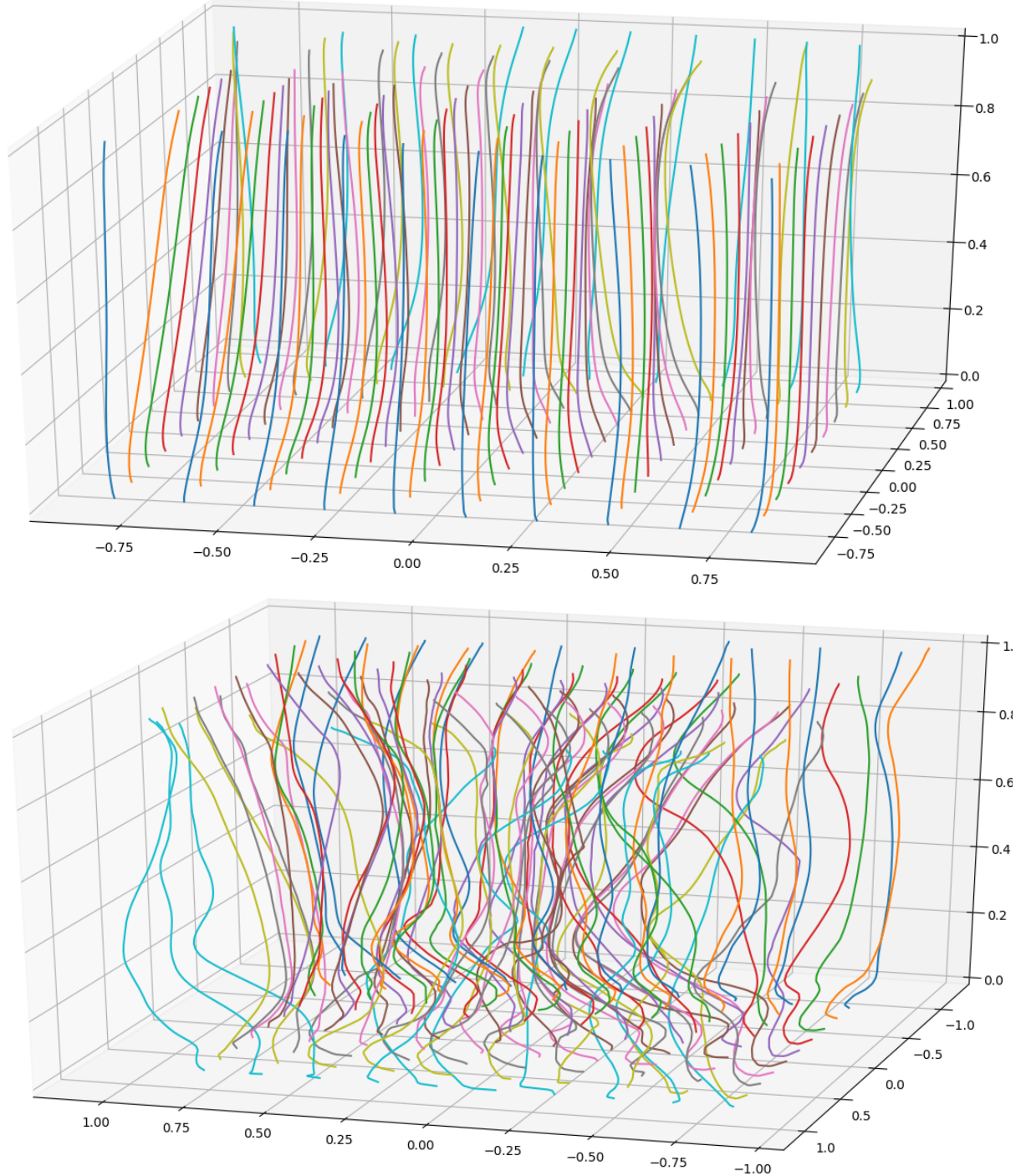


FIGURE F.2. Visualization of geodesic curves between two fibers isomorphic to  $[-1, 1]^2$ . Top: From  $F_4$  to  $F_9$ . Bottom: From  $F_1$  to  $F_0$ . With  $z$  being the height coordinate, the  $z = 0$  plane represents the starting fiber, while the  $z = 1$  plane represents the destination fiber. Clearly geodesics between  $F_0$  and  $F_1$  are less straight than between  $F_4$  and  $F_9$ . This suggests that the naive correspondence is not as strong, in accordance with intuition, and that  $F_1$  and  $F_0$  should not be naively identified.

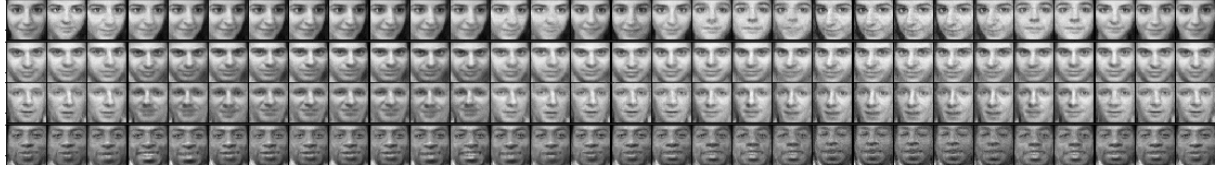


FIGURE F.3. Manifold plots of 30 generated images generated using an evenly spaced grid for naive transport. Each person is a condition and  $F = [-1, 1]$ . The original dataset contains only 10 examples per person. We see that naive transport places face of similar angles at similar positions in  $F$

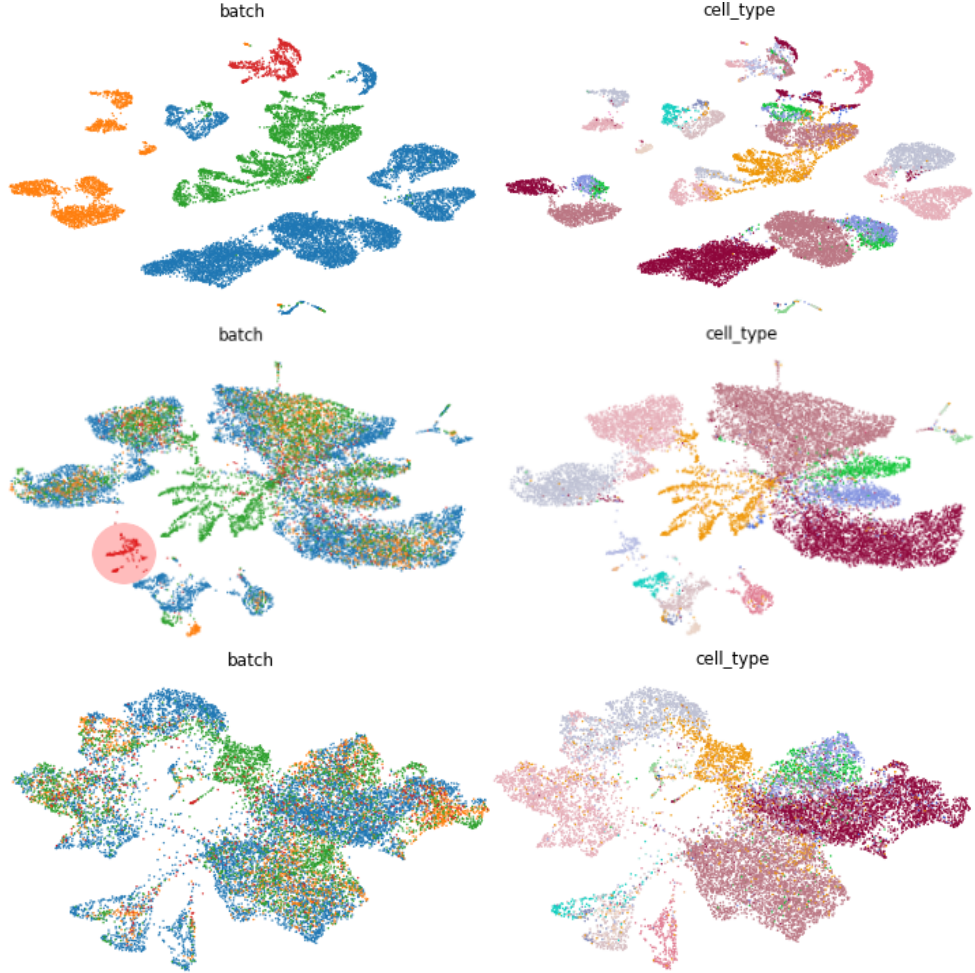


FIGURE F.4. UMAP visualization of pancreas cells. Left column: cells colored by batch, right: colored by cell types. From top to bottom: uncorrected data, scGen (bottleneck size: 100), naive transport (bottleneck size: 16). Contrary to scGen, naive transport was able to integrate cells from the red batch despite the small sample size. This suggests that FAE are better at integrating datasets of small sample sizes

## REFERENCES

[AAB<sup>+</sup>15] Martín Abadi, Ashish Agarwal, Paul Barham, Eugene Brevdo, Zhifeng Chen, Craig Citro, Greg S. Corrado, Andy Davis, Jeffrey Dean, Matthieu Devin, Sanjay Ghemawat, Ian Goodfellow, Andrew Harp, Geoffrey Irving, Michael Isard, Yangqing Jia, Rafal Jozefowicz, Lukasz Kaiser, Manjunath Kudlur, Josh Levenberg, Dan Mané, Rajat Monga, Sherry Moore, Derek Murray, Chris Olah, Mike Schuster, Jonathon Shlens, Benoit Steiner, Ilya Sutskever, Kunal Talwar, Paul Tucker, Vincent Vanhoucke, Vijay Vasudevan, Fernanda Viégas, Oriol Vinyals, Pete Warden, Martin Wattenberg, Martin Wicke, Yuan Yu, and Xiaoqiang Zheng. TensorFlow: Large-scale machine learning on heterogeneous systems, 2015. Software available from tensorflow.org.

[ACB17] Martin Arjovsky, Soumith Chintala, and Léon Bottou. Wasserstein generative adversarial networks. In *International conference on machine learning*, pages 214–223, 2017.

[AVDS<sup>+</sup>19] Matthew Amodio, David Van Dijk, Krishnan Srinivasan, William S Chen, Hussein Mohsen, Kevin R Moon, Allison Campbell, Yujiao Zhao, Xiaomei Wang, Manjunatha Venkataswamy, et al. Exploring single-cell data with deep multitasking neural networks. *Nature methods*, pages 1–7, 2019.

[BBR<sup>+</sup>18] Mohamed Ishmael Belghazi, Aristide Baratin, Sai Rajeshwar, Sherjil Ozair, Yoshua Bengio, Aaron Courville, and Devon Hjelm. Mutual information neural estimation. In *International Conference on Machine Learning*, pages 531–540, 2018.

[BLPL07] Yoshua Bengio, Pascal Lamblin, Dan Popovici, and Hugo Larochelle. Greedy layer-wise training of deep networks. In *Advances in neural information processing systems*, pages 153–160, 2007.

[Cut13] Marco Cuturi. Sinkhorn distances: Lightspeed computation of optimal transport. In *Advances in neural information processing systems*, pages 2292–2300, 2013.

[Dac07] Bernard Dacorogna. *Direct methods in the calculus of variations*, volume 78. Springer Science & Business Media, 2007.

[DFDC<sup>+</sup>18] Tim R Davidson, Luca Falorsi, Nicola De Cao, Thomas Kipf, and Jakub M Tomczak. Hyperspherical variational auto-encoders. *arXiv preprint arXiv:1804.00891*, 2018.

[GHL90] Sylvestre Gallot, Dominique Hulin, and Jacques Lafontaine. *Riemannian geometry*, volume 2. Springer, 1990.

[GL14] Yaroslav Ganin and Victor Lempitsky. Unsupervised domain adaptation by backpropagation. *arXiv preprint arXiv:1409.7495*, 2014.

[GPAM<sup>+</sup>14] Ian Goodfellow, Jean Pouget-Abadie, Mehdi Mirza, Bing Xu, David Warde-Farley, Sherjil Ozair, Aaron Courville, and Yoshua Bengio. Generative adversarial nets. In *Advances in neural information processing systems*, pages 2672–2680, 2014.

[GSSG12] Boqing Gong, Yuan Shi, Fei Sha, and Kristen Grauman. Geodesic flow kernel for unsupervised domain adaptation. In *2012 IEEE Conference on Computer Vision and Pattern Recognition*, pages 2066–2073. IEEE, 2012.

[GUA<sup>+</sup>17] Yaroslav Ganin, Evgeniya Ustinova, Hana Ajakan, Pascal Germain, Hugo Larochelle, François Laviolette, Mario Marchand, and Victor Lempitsky. Domain-adversarial training of neural networks. In *Domain Adaptation in Computer Vision Applications*, pages 189–209. Springer, 2017.

[IT01] Jin-ichi Itoh and Minoru Tanaka. The lipschitz continuity of the distance function to the cut locus. *Transactions of the American Mathematical Society*, 353(1):21–40, 2001.

[KB14] Diederik P Kingma and Jimmy Ba. Adam: A method for stochastic optimization. *arXiv preprint arXiv:1412.6980*, 2014.

[KLA19] Tero Karras, Samuli Laine, and Timo Aila. A style-based generator architecture for generative adversarial networks. In *Proceedings of the IEEE Conference on Computer Vision and Pattern Recognition*, pages 4401–4410, 2019.

[KMF<sup>+</sup>19] Ilya Korsunsky, Nghia Millard, Jean Fan, Kamil Slowikowski, Fan Zhang, Kevin Wei, Yuriy Baglaenko, Michael Brenner, Po-ru Loh, and Soumya Raychaudhuri. Fast, sensitive and accurate integration of single-cell data with harmony. *Nature methods*, pages 1–8, 2019.

[KMRW14] Durk P Kingma, Shakir Mohamed, Danilo Jimenez Rezende, and Max Welling. Semi-supervised learning with deep generative models. In *Advances in neural information processing systems*, pages 3581–3589, 2014.

[KSM99] Ivan Kolár, Jan Slovák, and Peter W Michor. Natural operations in differential geometry. 1999.

[KST<sup>+</sup>18] Hyun Min Kang, Meena Subramaniam, Sasha Targ, Michelle Nguyen, Lenka Maliskova, Elizabeth McCarthy, Eunice Wan, Simon Wong, Lauren Byrnes, Cristina M Lanata, et al. Multiplexed droplet single-cell rna-sequencing using natural genetic variation. *Nature biotechnology*, 36(1):89, 2018.

[LC10] Yann LeCun and Corinna Cortes. MNIST handwritten digit database. 2010.

[LCC<sup>+</sup>17] Chun-Liang Li, Wei-Cheng Chang, Yu Cheng, Yiming Yang, and Barnabás Póczos. Mmd gan: Towards deeper understanding of moment matching network. In *Advances in Neural Information Processing Systems*, pages 2203–2213, 2017.

[LNTW19] Mohammad Lotfollahi, Mohsen Naghipourfar, Fabian J Theis, and F Alexander Wolf. Conditional out-of-sample generation for unpaired data using trvae. *arXiv preprint arXiv:1910.01791*, 2019.

[LSLW15] Anders Boesen Lindbo Larsen, Søren Kaae Sønderby, Hugo Larochelle, and Ole Winther. Autoencoding beyond pixels using a learned similarity metric. *arXiv preprint arXiv:1512.09300*, 2015.

[LWT19] Mohammad Lotfollahi, F Alexander Wolf, and Fabian J Theis. scgen predicts single-cell perturbation responses. *Nature methods*, 16(8):715–721, 2019.

[MHM18] Leland McInnes, John Healy, and James Melville. Umap: Uniform manifold approximation and projection for dimension reduction. *arXiv preprint arXiv:1802.03426*, 2018.

[MO14] Mehdi Mirza and Simon Osindero. Conditional generative adversarial nets. *arXiv preprint arXiv:1411.1784*, 2014.

[MSJ<sup>+</sup>15] Alireza Makhzani, Jonathon Shlens, Navdeep Jaitly, Ian Goodfellow, and Brendan Frey. Adversarial autoencoders. *arXiv preprint arXiv:1511.05644*, 2015.

[Nic19] Nicki Skafte Detlefsen and Soren Hauberg. Explicit disentanglement of appearance and perspective in generative models. In *Advances in Neural Information Processing Systems (NeurIPS)*, 2019.

[Ode16] Augustus Odena. Semi-supervised learning with generative adversarial networks. *arXiv preprint arXiv:1606.01583*, 2016.

[PGC<sup>+</sup>17] Adam Paszke, Sam Gross, Soumith Chintala, Gregory Chanan, Edward Yang, Zachary DeVito, Zeming Lin, Alban Desmaison, Luca Antiga, and Adam Lerer. Automatic differentiation in pytorch. 2017.

[PSF19] Xavier Pennec, Stefan Sommer, and Tom Fletcher. *Riemannian Geometric Statistics in Medical Image Analysis*. Academic Press, 2019.

[PVG<sup>+</sup>11] Fabian Pedregosa, Gaël Varoquaux, Alexandre Gramfort, Vincent Michel, Bertrand Thirion, Olivier Grisel, Mathieu Blondel, Peter Prettenhofer, Ron Weiss, Vincent Dubourg, et al. Scikit-learn: Machine learning in python. *Journal of machine learning research*, 12(Oct):2825–2830, 2011.

[Sap06] Gilbert Saporta. *Probabilités, analyse des données et statistique*. Editions Technip, 2006.

[TAC<sup>+</sup>20] Hoa Thi Nhu Tran, Kok Siong Ang, Marion Chevrier, Xiaomeng Zhang, Nicole Yee Shin Lee, Michelle Goh, and Jinmiao Chen. A benchmark of batch-effect correction methods for single-cell rna sequencing data. *Genome Biology*, 21(1):1–32, 2020.

[Tri10] Hans Triebel. *Bases in function spaces, sampling, discrepancy, numerical integration*, volume 11. European Mathematical Society, 2010.

[Vil08] Cédric Villani. *Optimal transport: old and new*, volume 338. Springer Science & Business Media, 2008.

[VLL<sup>+</sup>10] Pascal Vincent, Hugo Larochelle, Isabelle Lajoie, Yoshua Bengio, and Pierre-Antoine Manzagol. Stacked denoising autoencoders: Learning useful representations in a deep network with a local denoising criterion. *Journal of machine learning research*, 11(Dec):3371–3408, 2010.

[WSL17] Liwei Wang, Alexander Schwing, and Svetlana Lazebnik. Diverse and accurate image description using a variational auto-encoder with an additive gaussian encoding space. In *Advances in Neural Information Processing Systems*, pages 5756–5766, 2017.

[XD18] Jiacheng Xu and Greg Durrett. Spherical latent spaces for stable variational autoencoders. *arXiv preprint arXiv:1808.10805*, 2018.

[ZPIE17] Jun-Yan Zhu, Taesung Park, Phillip Isola, and Alexei A Efros. Unpaired image-to-image translation using cycle-consistent adversarial networks. In *Proceedings of the IEEE international conference on computer vision*, pages 2223–2232, 2017.